Mineralogy of Juventae Chasma: Sulfates in the light-toned mounds, mafic minerals in the bedrock, and hydrated silica and hydroxylated ferric sulfate on the plateau

Janice L. Bishop,[1,2] Mario Parente,[3] Catherine M. Weitz,[4] Eldar Z. Noe Dobrea,[5] Leah H. Roach,[6] Scott L. Murchie,[7] Patrick C. McGuire,[8,9,10] Nancy K. McKeown,[11] Christopher M. Rossi,[12] Adrian J. Brown,[1,2] Wendy M. Calvin,[13] Ralph Milliken,[5] and John F. Mustard[6]

Received 30 January 2009; revised 1 July 2009; accepted 17 July 2009; published 19 November 2009.

[1] Juventae Chasma contains four light-toned sulfate-bearing mounds (denoted here as A–D from west to east) inside the trough, mafic outcrops at the base of the mounds and in the wall rock, and light-toned layered deposits of opal and ferric sulfates on the plateau. Hyperspectral visible/near-infrared Compact Reconnaissance Imaging Spectrometer for Mars (CRISM) spectra were used to identify monohydrated and polyhydrated sulfate (PHS) outcrops of layered material on the bright mounds. Most of the monohydrated sulfate signatures closely resemble those of szomolnokite ($FeSO_4 \cdot H_2O$), characterized by a water band near 2.08 μm, while some areas exhibit spectral features more similar to those of kieserite ($MgSO_4 \cdot H_2O$), with a band centered closer to 2.13 μm. The largest PHS outcrops occur on the top of mound B, and their spectral features are most consistent with ferricopiapite, melanterite, and starkeyite, but a specific mineral cannot be uniquely identified at this time. Coordinated analyses of CRISM maps, Mars Orbiter Laser Altimeter elevations, and High Resolution Imaging Science Experiment images suggest that mounds A and B may have formed together and then eroded into separate mounds, while mounds C and D likely formed separately. Mafic minerals (low-Ca pyroxene, high-Ca pyroxene, and olivine) are observed in large ~2–10 km wide outcrops in the wall rock and in smaller outcrops ~50–500 m across at the floor of the canyon. Most of the wall rock is covered by at least a thin layer of dust and does not exhibit strong features characteristic of these minerals. The plateau region northwest of Juventae Chasma is characterized by an abundance of light-toned layered deposits. One region contains two spectrally unique phases exhibiting a highly stratified, terraced pattern. CRISM spectra of one unit eroded into swirling patterns with arc-like ridges exhibit a narrow 2.23-μm band assigned to hydroxylated ferric sulfate. A thin layer of a fractured material bearing an opaline silica phase is observed at the contact between the older plateau unit and the younger hydroxylated ferric sulfate-bearing light-toned layered deposits. Hydrothermal processes may have produced an acidic environment that fostered formation of the hydrated silica and hydroxylated ferric sulfate units.

Citation: Bishop, J. L., et al. (2009), Mineralogy of Juventae Chasma: Sulfates in the light-toned mounds, mafic minerals in the bedrock, and hydrated silica and hydroxylated ferric sulfate on the plateau, *J. Geophys. Res.*, *114*, E00D09, doi:10.1029/2009JE003352.

[1]Carl Sagan Center, SETI Institute, Mountain View, California, USA.
[2]NASA Ames Research Center, Mountain View, California, USA.
[3]Department of Electrical Engineering, Stanford University, Stanford, California, USA.
[4]Planetary Science Institute, Tucson, Arizona, USA.
[5]Jet Propulsion Laboratory, California Institute of Technology, Pasadena, California, USA.
[6]Department of Geological Sciences, Brown University, Providence, Rhode Island, USA.
[7]Johns Hopkins University Applied Physics Laboratory, Laurel, Maryland, USA.
[8]Department of Planetary Science and Remote Sensing, Freie Universitaet, Berlin, Germany.
[9]Institute of Planetary Research, German Aerospace Center, Berlin, Germany.
[10]Formerly at McDonnell Center for the Space Sciences, Washington University, St. Louis, Missouri, USA.
[11]Department of Earth and Planetary Sciences, University of California, Santa Cruz, California, USA.
[12]Department of Aerospace Engineering, University of Michigan, Ann Arbor, Michigan, USA.
[13]Department of Geological Sciences and Engineering, University of Nevada, Reno, Nevada, USA.

0148-0227/09/2009JE003352

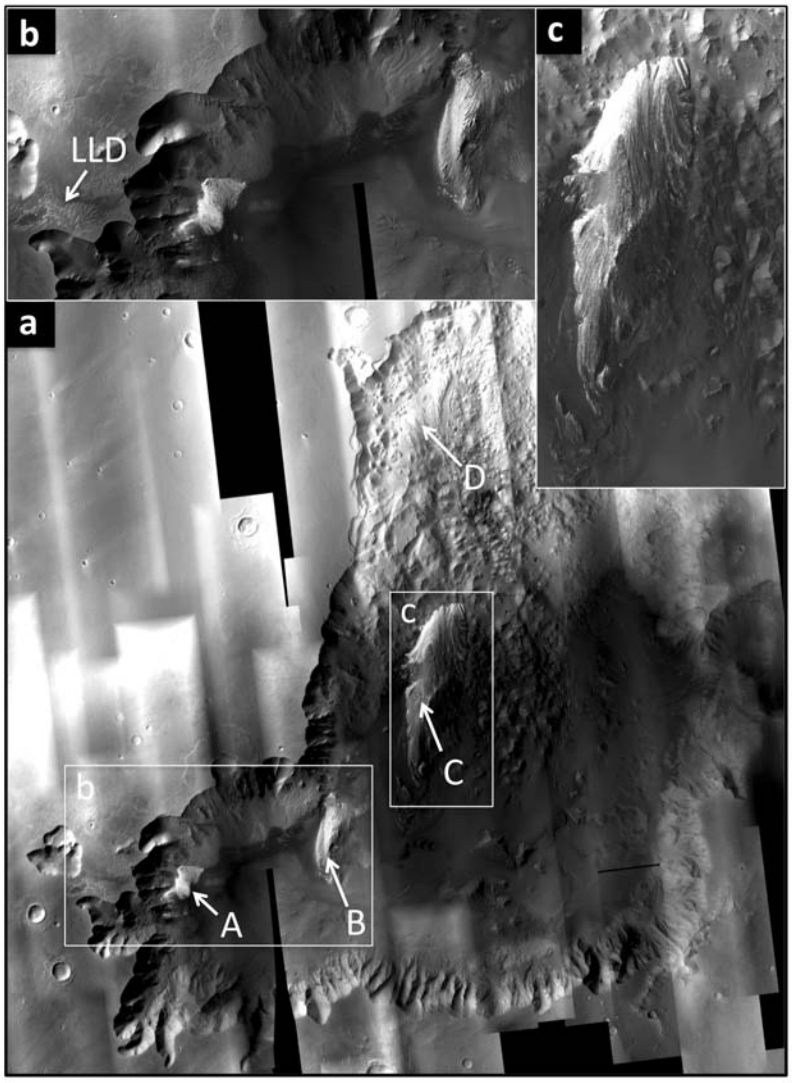

Figure 1. (a) CTX mosaic of Juventae Chasma with mounds A, B, C, and D marked, (b) an expanded view of mounds A and B and the plateau LLD study region, and (c) an expanded view of mound C.

1. Introduction

[2] Light-toned outcrops have been studied recently in Juventae Chasma using Mars Global Surveyor (MGS), Mars Orbiter Camera (MOC) and Mars Odyssey Thermal Emission Imaging System (THEMIS) images [*Chapman et al.*, 2003; *Catling et al.*, 2006]. These interior layered deposits (ILDs) at Juventae are labeled mounds A, B, C, and D moving from W to E in the basin toward the outflow at Maja Vallis (Figure 1) [*Chapman et al.*, 2003; *Catling et al.*, 2006]. Light-toned layered deposits (LLDs) are also found on the plateau west of the chasma [*Treiman et al.*, 1995; *Lucchitta and Chapman*, 2002; *Mangold et al.*, 2008; *Weitz et al.*, 2008]. Hyperspectral images collected by the Observatoire pour la Minéralogie, l'Eau, les Glaces, et l'Activité (OMEGA) on board Mars Express show hydrated sulfates present in mounds A, B, and C [*Gendrin et al.*, 2005].

[3] Mars Reconnaissance Orbiter (MRO) Compact Reconnaissance Imaging Spectrometer for Mars (CRISM) spectra of these sulfate mounds enable more precise characterization of the types of sulfate minerals present. CRISM analyses of Juventae Chasma also reveal small outcrops of mafic minerals in bedrock showing through the sand and dust at the base of the sulfate mounds [*Bishop et al.*, 2007a]. On the plateau to the northwest of Juventae Chasma are a series of light-toned layered deposits and inverted channels [*Treiman et al.*, 1995; *Lucchitta and Chapman*, 2002; *Weitz et al.*, 2008, 2009]. CRISM has identified two types of hydrated material present in this region: opaline silica/altered silica glass and partially dehydrated ferric sulfate [*Milliken et al.*, 2008]. Here we present a study of the sulfate minerals found in the bright mounds or ILDs, the mafic minerals found in the small bedrock outcrops near the mounds and the large bedrock outcrops in the wall rock, and hydrated materials found in the LLDs on the plateau adjacent to the chasma. Coordinated analyses of composition from CRISM spectra and surface morphologies and textures from the MRO High Resolution Imaging Science Experiment

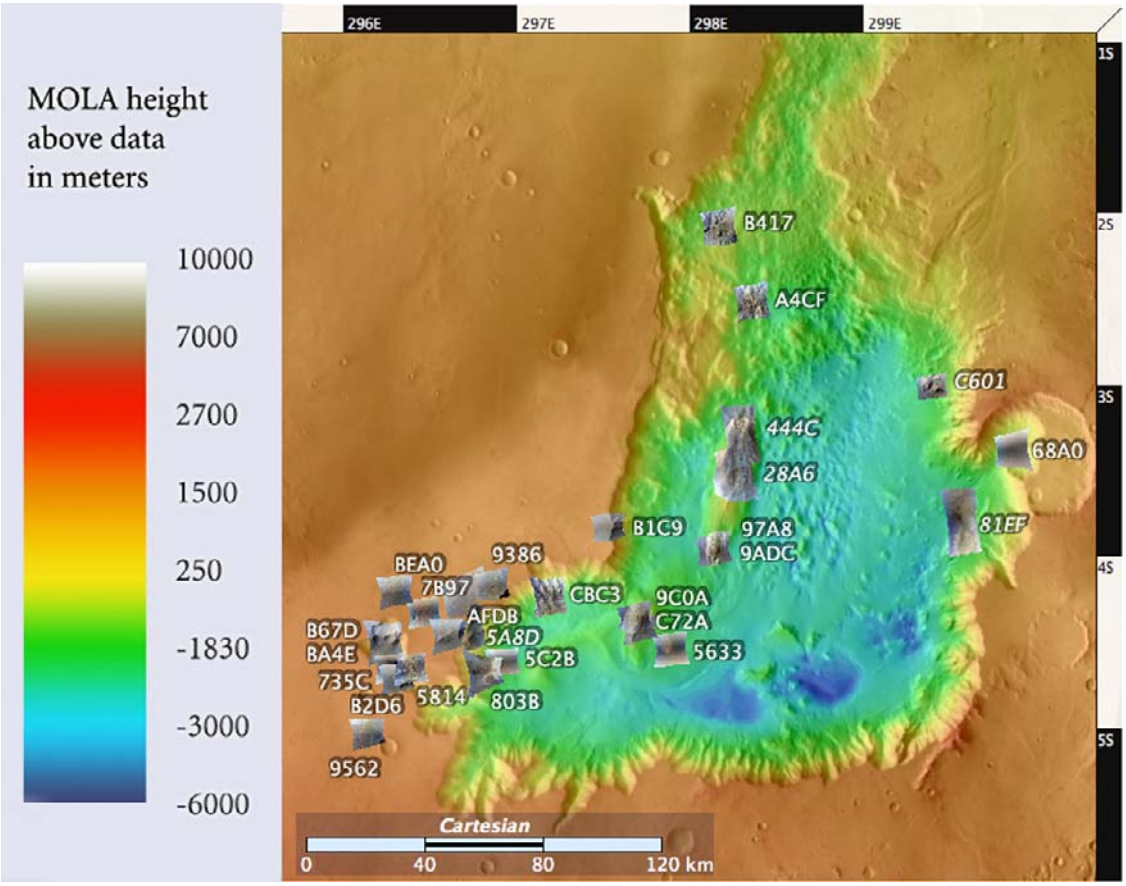

Figure 2. THEMIS-MOLA mosaic of the Juventae Chasma region with CRISM image footprints overlain using MR PRISM code [*Brown and Storrie-Lombardi*, 2006].

(HiRISE) provide insights into the nature of the light-toned deposits and their formation processes.

2. Background

2.1. Light-Toned Deposits at Juventae Chasma

[4] Juventae Chasma is a 3 km deep depression about 150 km wide located near 4°S and 298°E. It is associated with the Valles Marineris system, but is separated from the main channel by 500 km. A THEMIS/IR daytime mosaic overlain with Mars Orbiter Laser Altimeter (MOLA) color gridded topography of Juventae Chasma in Figure 2 shows the CRISM image footprints, the striking elevation changes at the chasma walls, and the deepest portion of the chasma in the SE. The chasma likely formed due to stresses related to the Tharsis rise during the late Noachian to early Hesperian period [e.g., *Lucchitta et al.*, 1992; *Chapman et al.*, 2003]. Crater counts suggest that the final flood event may have occurred during the Amazonian period [*Chapman et al.*, 2003].

[5] A more detailed view of the light-toned deposits and chaotic terrain is shown in images taken by the Context Camera (CTX) on board MRO, mosaicked together in Figure 1. ILDs are found in mounds A, B, C, and D as identified in earlier studies [*Chapman et al.*, 2003; *Catling et al.*, 2006], and LLDs are found on the plateau region NW of the chasma [*Mangold et al.*, 2008; *Milliken et al.*, 2008; *Weitz et al.*, 2008]. High-Resolution Stereo Camera (HRSC) images of the western part of the chasma and plateau are shown in Figure 3. Analyses of HRSC images of the ILDs suggest a sedimentary origin for the mounds [*Hauber et al.*, 2004; *Michael et al.*, 2005; *Ori et al.*, 2006]. Other studies suggest they are lacustrine deposits [*McCauley*, 1978; *Peterson*, 1981], subaerial volcanoes [*Peterson*, 1981; *Lucchitta*, 1990], dust deposits on ice-covered lakes [*Nedell et al.*, 1987], subice volcanoes deposited in meltwater [*Chapman and Tanaka*, 2001; *Komatsu et al.*, 2004], or large-scale spring deposits [*Rossi et al.*, 2008]. Figure 3 shows the branching and bifurcating spurs in the wall rock [*Lucchitta et al.*, 1992; *McEwen et al.*, 1999] and the bright ILDs that are partially covered by dark sand in the chasma. A better view of the terrain is shown in Movie 1 where the dark sand contrasts greatly with the bright material of mounds A and B.

[6] These bright mounds unconformably overlie chaotic terrain on the canyon floor [*Komatsu et al.*, 1993] and rise kilometers above the canyon floor: ~2 km for mound A, ~2.8 km for mound B, and ~3.3 km for mound C [*Catling et al.*, 2006]. The relationship of large bright Juventae mounds overlying floor deposits was also noted by *Chapman and Tanaka* [2001] and *Chapman* [2002]. In addition, another small bright mound northeast of mound C was shown to underlie chaotic terrain [i.e., *Chapman et al.*, 2003, Figure 4e]. *Catling et al.* [2006] applied analyses of MOC, MOLA, and THEMIS thermal inertia data toward understanding these light-toned deposits and suggested

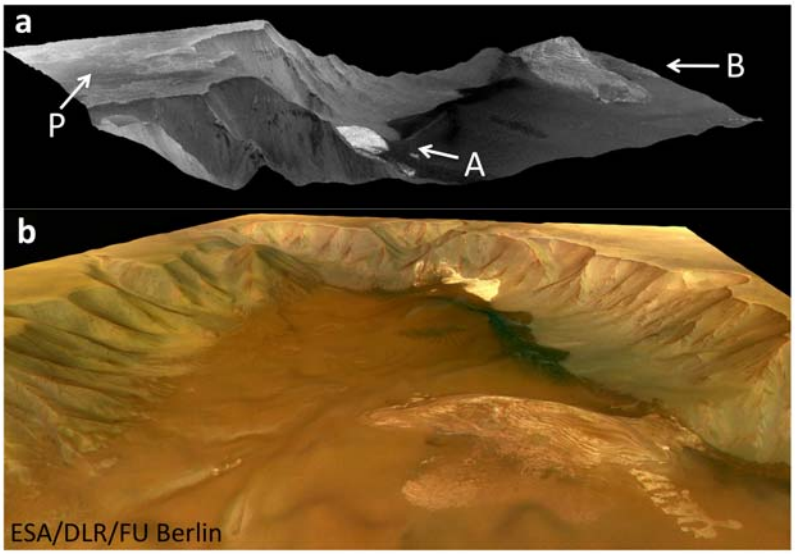

Figure 3. Topography of western Juventae Chasma: (a) The NADIR panchromatic channel of HRSC image H0243_0000 projected over an HRSC DEM in equirectangular coordinates showing mounds A and B and the LLD on the plateau marked with P, and (b) 3-D HRSC mosaic 0583D301 showing ILD material at mounds A and B, dark sand filling in most of the chasma floor, and the steep slopes of the chasma walls (image credit: ESA/DLR/FU Berlin/G. Neukum).

three possible formation scenarios: (1) volcanic deposition, (2) sedimentary deposition, or (3) aeolian deposition. They considered volcanic emplacement (described in previous studies) [e.g., *Chapman et al.*, 2003] less likely and favored hypotheses where liquid water was actively involved. Analyses of the LLDs along the plateau suggest aqueous processes are responsible for their formation [*Weitz et al.*, 2008] and that the LLDs result from deposition in a subaerial environment [*Le Deit et al.*, 2009].

2.2. Light-Toned Deposits at Valles Marineris

[7] ILDs were observed throughout the broader region of Valles Marineris first using Mariner 9 images [*Sharp*, 1973; *McCauley*, 1978], and Viking images [*Peterson*, 1981; *Lucchitta*, 1982; *Nedell et al.*, 1987; *Lucchitta et al.*, 1992, 1994; *Komatsu et al.*, 1993], then in more detail using MOC and THEMIS images [*Chapman and Tanaka*, 2001; *Malin and Edgett*, 2001; *Weitz et al.*, 2001; *Chapman*, 2002; *Chapman and Tanaka*, 2002; *Komatsu et al.*, 2004; *Chapman and Smellie*, 2007]. Debris accumulations and ripples are commonly observed on top of the ILDs in the Valles Marineris region, typically leaving only small dust-free areas that are well below the 3-km Thermal Emission Spectrometer (TES) resolution [*Weitz et al.*, 2001; *Chapman*, 2002]; perhaps explaining why TES signatures of this region are dominated by basaltic features [*Christensen et al.*, 2001]. *Lucchitta* [1990] described the emplacement of these ILDs as the last major event in the formation of the Valles Marineris system and advocated a volcanic origin for these deposits. *Nedell et al.* [1987] described possible geologic processes that could have formed these ILD deposits through ice-covered paleolakes.

[8] Combined CRISM/HiRISE studies are also investigating ILDs in Valles Marineris where sulfates are present [*Murchie et al.*, 2009a; *Roach et al.*, 2009a, 2009b]. The study of layered deposits at eastern Candor Chasma found alternating layers of monohydrated sulfates and polyhydrated sulfates (PHS) on many slopes of the layered deposits [*Roach et al.*, 2009a]. Analysis of the western Candor Chasma deposits identified primarily monohydrated sulfates in lower (older) sediments and polyhydrated sulfates in higher (younger) sediments [*Murchie et al.*, 2009a]. The latter study also includes hydrologic modeling of the Tharsis region that suggests a regional geologic process may account for emplacement of sulfate- and iron oxide–bearing sediments in both the Valles Marineris and the Meridiani Planum regions. They propose that sulfate salts formed by evaporation of groundwater that discharged trapped aeolian sediments subsequently formed the sulfate and iron oxide minerals observed.

2.3. LLDs at Juventae Chasma Plateau

[9] The LLDs on the plateau region northwest of Juventae are characterized by narrow sinuous lineations ~20–200 m wide with lengthy paths up to tens of kilometers [*Lucchitta*, 2005; *Mangold et al.*, 2008]. The branching pattern of many of these features is consistent with fluvial channels. Analysis of HRSC images in the Valles Marineris region found the presence of many related LLDs at Juventae, Ius, Melas, and Ganges Chasma and several other chasmata in the Valles Marineris region [*Le Deit et al.*, 2008]. They found a polygonal texture in the LLDs at Juventae Chasma and interbedding of the LLDs with darker materials. More recent analyses of the LLDs on the plateau using MRO/HiRISE and CRISM data indicate variations in brightness, color, fracturing and erosional properties that are distinct from the ILDs within the chasma and imply sustained periods of water flow on the plateau during the Hesperian period [*Weitz et al.*, 2008]. Compositional analyses of the LLDs using CRISM data indicate the presence of opaline silica and partially dehydrated iron sulfates [*Milliken et al.*, 2008; *Weitz et al.*, 2009].

Table 1. List of CRISM Summary Parameters Used in This Study[a]

Parameter	Formula	Measurement
BD1900	1 − (((R1930 + R1985) * 0.5)/(a * R1857 + b * R2067))	Band depth at 1.9 μm
BD2100	1 − (((R2120 + R2140) * 0.5)/(a * R1930 + b * R2250))	Band depth at 2.1 μm
BD2210	1 − (R2210/(a * R2140 + b * R2250))	Band depth at 2.21 μm
BD2230	1 − ((b1 + b2)/((b3 + b4 + b5 + b6) * 0.25)); b1 = 2.2120, b2 = 2.2252, b3 = 2.1129, b4 = 2.1261, b5 = 2.3575, b6 = 2.3707 μm	Band depth at 2.23 μm
SINDEX	1 − ((R2100 + R2400)/(2 * R2290))	Convexity near 2.3 μm
OLINDEX	(R1695/(0.1 * R1050 + 0.1 * R1210 + 0.4 * R1330 + 0.4 * R1470)) − 1	Positive slope from 1 to 1.5 μm
LCPINDEX	((R1330 − R1050)/(R1330 + R1050)) * ((R1330 − R1815)/(R1330 + R1815)	Convexity near 1.3 μm
HCPINDEX	((R1470 − R1050)/(R1470 + R1050)) * ((R1470 − R2067)/(R1470 + R2067)	Convexity near 1.5 μm

[a]The BD2230 parameter is from *Milliken et al.* [2008]; all other parameters are from *Pelkey et al.* [2007]. In these parameters, a = 1 − b and b = (λC − λS)/(λL − λS), where "C" is the center of the band being measured and "S" and "L" are shorter and longer wavelength continuum points, respectively. "R1930" represents the reflectance value at 1930 nm, etc.

[10] *Mangold et al.* [2008] characterized valley or channel systems associated with the layered deposits in the plateau adjacent to Juventae Chasma using HRSC images. *Weitz et al.* [2008, 2009] studied these deposits in additional detail using HiRISE images and identified valley or channel systems associated with layered deposits in the plateau regions adjacent to Juventae Chasma, as well as other plateau regions adjacent to Ius, Melas, Candor, and Ganges Chasmata. These studies also found that the valleys, channels, and light-toned layered units along the Juventae wall are most likely coincident with the aqueous activity that produced and affected similar features on the adjacent plateau. Analysis of the LLDs on the plateau next to these chasmata also suggests that the hydrological activity occurred after formation of the associated chasmata. The strong correlation between fluvial landforms and LLDs surrounding these chasmata argues for sustained precipitation, surface runoff, and fluvial deposition occurring during the late Hesperian or early Amazonian on the Valles Marineris plateau and along portions of the Juventae Chasma wall [*Mangold et al.*, 2008; *Weitz et al.*, 2009].

3. Methods

3.1. Preprocessing of CRISM Data

[11] CRISM acquires images in a high-resolution targeted mode and a lower-resolution mapping mode using two detectors: a VNIR detector covering the spectral range 0.36–1.05 μm and an IR detector covering 1.00–3.92 μm [*Murchie et al.*, 2007, 2009b]. Full resolution targeted (FRT) images include 544 channels across the full spectral range from 0.36 to 3.92 μm with a spectral sampling of 6.5 nm, in ~10–12 km wide swaths at ~18 m/pixel. Half resolution long (HRL) images have the same spectral resolution as the FRT images, but are binned spatially resulting in ~40 m/pixel spatial resolution. The multispectral mapping (MSP) images include 72 narrow channels from 0.36 to 3.92 μm that were selected to identify diagnostic mineralogical and atmospheric features and have either ~100 or 200 m/pixel spatial resolution.

[12] CRISM data are processed using steps developed and revised by the team over the first Mars year [*Murchie et al.*, 2009b]. Briefly, the CRISM data are converted to I/F by subtracting the instrument background, dividing by processed measurements of the internal calibration standard, and dividing by solar irradiance. Variations in illumination are corrected by dividing the resulting I/F by the cosine of the incidence angle (derived from MOLA gridded topography at 128 pixels per degree). The effects of atmospheric molecular opacity are minimized by dividing by a scaled atmospheric transmission spectrum derived from multiple observations over Olympus Mons. Images are then processed using a cleaning algorithm to remove noise and large spikes within the data due to instrument effects [*Parente*, 2008]. Band math calculations are performed to create a set of spectral parameters that highlight specific features associated with mineral types [*Pelkey et al.*, 2007]. Those used for this study are summarized in Table 1. A suite of similar mineral parameter images are available online at http://crism-map.jhuapl.edu/. Finally, the images from the VNIR and IR detectors are spliced together to enable examination of complete CRISM spectra (M. Parente et al., Decomposition of mineral absorption bands using nonlinear least squares curve fitting: Applications to Martian meteorite and CRISM data, submitted to *Remote Sensing Environment*, 2009). The images used for spectral analyses in this study are listed in Table 2.

3.2. Mineral Identification With CRISM Data

[13] The signature of monohydrated sulfates is so pervasive in many of the CRISM images that it was difficult to find a "spectrally unremarkable" spot for ratioing the sulfate spectra, as is frequently performed in order to enhance the spectral features of interest [*Murchie et al.*,

Table 2. List of CRISM and HiRISE Images Used in This Study

CRISM	HiRISE
Map tile MC18/T0934	Mound A: PSP_004291_1755, PSP_005557_1755
Mound A: FRT00005C2B, FRT0000803B	Mound B: PSP_007126_1755
Mound B: FRT00005633, FRT00009C0A	Mound C: PSP_002946_1765, PSP_006915_1760
Mound C: FRT0000444C, FRT000097A8, FRT00009ADC	Plateau: PSP_003434_1755
Mound D: FRT0000A4CF	
Plateau: FRT00005814	

Table 3. Wavelengths Used for Band Depth Calculations in Elevation Determinations Shown in Figure 8[a]

Band Depth	Short Wavelength	Middle Wavelength	High Wavelength
2.06/2.09	2.00	2.06–2.09	2.21
2.13	2.11	2.13–2.14	2.16

[a]All wavelengths in μm.

2009b]. In fact, we often found that spectral artifacts were created when ratios were attempted. Furthermore, in some cases ratioing a spectrum of a region dominated by PHS to a spectrum containing monohydrated sulfate created the artificial appearance of a gypsum-like band near 2.2 μm. For this reason, we have opted to avoid ratio spectra for the sulfate-bearing spectra presented here, although that means that there is a larger degree of noise due to instrument effects and atmospheric components than would be present using ratioed spectra.

[14] The distributions of the monohydrated sulfates kieserite and szomolnokite were determined using two methods of mineral identification followed by comparison with elevation data from MOLA Mission Experiment Gridded Data Records (MEGDRs), which are binned to 128 pixels per degree (approximately 462 m/pixel) [*Smith et al.*, 2001]. 50 m/pixel topographic data from HRSC on ESA's Mars Express Mission [*Ansan et al.*, 2008] were used as well where available. Kieserite and szomolnokite were mapped via both parameters (using variations of the ~2.1-μm band shape) and end-member unmixing of the scene (using manually identified spectral end-members). The two mapping methods provided self-consistent results, lending credence to the robustness of our technique. Band parameterization took advantage of the differences in the ~2.1-μm band between kieserite and szomolnokite. Kieserite spectra exhibit a doublet at 2.06 and 2.13 μm, whereas szomolnokite spectra have a singlet at 2.09 μm. We therefore calculated two band depths: one for the location of the minimum associated with either of these monohydrated sulfates (allowing the code to determine the location of the band minimum in the 2.06–2.09 μm region), and one for the 2.13 μm absorption associated with kieserite (Table 3). In these calculations band depth is defined as $1 - ([a + c]/2)/b$, where a and c are the I/F values at the continuum wavelengths encompassing the absorptions, and b is the I/F value at the wavelength of the band center. This method allowed us to identify kieserite in all places where both band depth maps presented values >3%, and szomolnokite in places where only the first band depth map presented values >3%. Relatively large band depths were used as weak bands are often found outside of the mound regions where sulfates have presumably been distributed with the dust. The mean, minimum, maximum, and standard deviation of the elevation were calculated for each compositional unit.

3.3. Camera Preprocessing

[15] All HiRISE images used in this study are NOMAP products with north oriented approximately 7° to the right of the top unless otherwise noted [*McEwen et al.*, 2007]. HiRISE false color images were made by displaying the IR, RED, and BG channels in red, green, and blue, respectively [*McEwen*, 2009]. For color images, each color band is individually stretched to maximize contrast, so the colors are enhanced differently for each image based on the color and brightness of each scene. HiRISE stereo pairs are produced by displaying the more left-looking image (smaller or more negative roll angle) in red and the more right-looking image in both green and blue. When viewed with red-blue glasses, the image appears as an anaglyph showing a three-dimensional view. A list of the HiRISE images used in this study is given in Table 2.

[16] The CTX data are corrected to 16-bit radiometrically calibrated (I/F) units using preflight radiometric, flat field and dark measurements. This processing does not account for changes in illumination due to off-nadir viewing geometry in some observations, nor from changing atmospheric conditions so that there can be variations in the absolute brightness levels between strips. Each image strip is map projected to a Mercator standard projection, in this case using longitude bounds of −5.765 and −1.975°N and latitude bounds of 64.05 and 59.95°W. Each projected strip is then mosaicked with the last pixel in the region of overlap and image edge smoothing was applied over the image boundaries. These calibration and projection routines are custom compiled binaries created at Malin Space Science Systems, based on algorithms developed for MOC, and distributed to the CTX team. Map projection accounts for predicted and actual values of the spacecraft orbit (SPICE kernels) as well as MOLA derived elevation of the sight. Additional information on the CTX camera is provided by *Malin et al.* [2007].

[17] HRSC images used here are shown using the panchromatic NADIR channel and were processed using level4 calibration and an equirectangular projection to coordinate with CRISM observations with respect to the MOLA aeroid, instead of the normal sinusoidal projection [*Neukum et al.*, 2004; *Jaumann et al.*, 2007]. Digital elevation model (DEM) production was performed here as in previous studies [*Gwinner et al.*, 2007, 2008]. The image in Figure 3b was prepared by the HRSC team.

[18] The map in Figure 2 was created by overlaying the THEMIS global map product in black and white and colorizing it according to MOLA data from the 256 ppd global MOLA product. Blue corresponds to low elevations and red to high elevations. The locations of CRISM footprints were overlain using the CRISM global shapefile for HRL, HRS and FRT targets. The CRISM images were represented using the "TRU" false color representation for CRISM standard data products produced by the JHU/APL CRISM Science Operations Center (available online at http://crism-map.jhuapl.edu/). This is a standard procedure in the MR PRISM software [*Brown and Storrie-Lombardi*, 2006].

4. Results

4.1. Mineralogic Trends at Juventae Chasma

[19] CRISM coverage over Juventae Chasma in the mapping mode is not yet complete, though the western region has the most coverage. Figure 4 shows three views of Juventae from map tile MC18/T0934. The production of the map tiles is described by *Murchie et al.* [2009b], with atmospheric, thermal and photometric correction as described by *McGuire et al.* [2008]. The false color RGB image (Figure 4a) shows the topography and light-toned

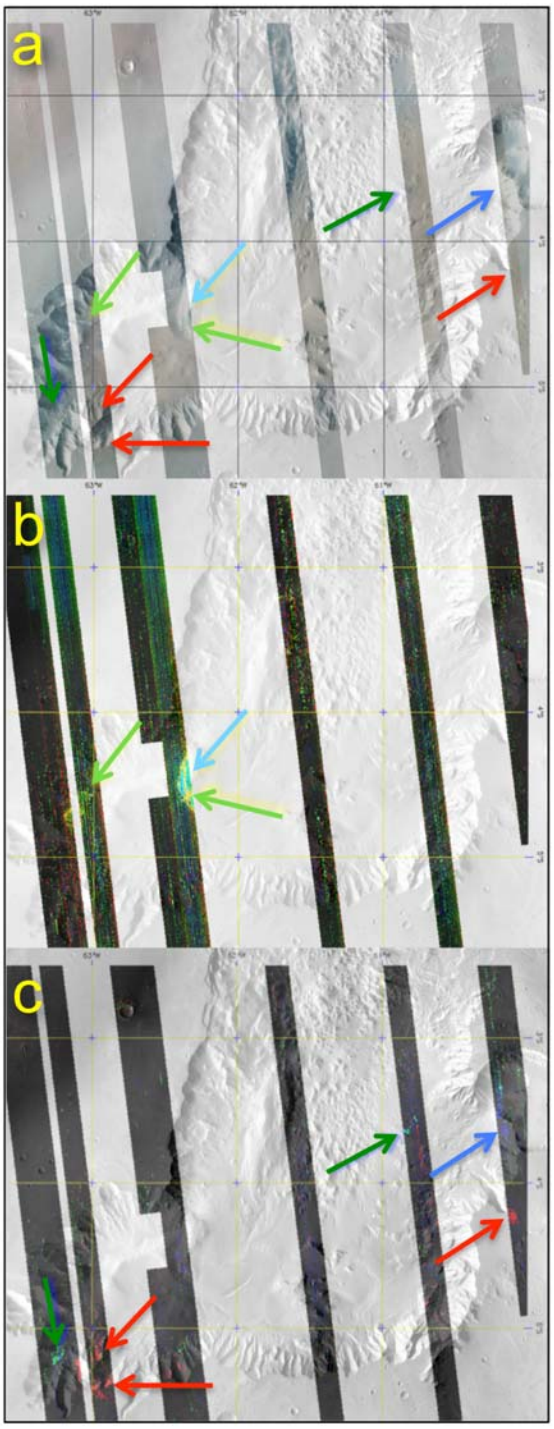

Figure 4. CRISM multispectral map of Juventae Chasma region on tile MC18/T0934 overlain on a THEMIS mosaic with key mineral signatures indicated by arrows: (a) mapped with R at 2.5 μm, G at 1.5 μm, and B at 1.08 μm with arrows marking features shown in Figures 4b and 4c, (b) mineral indicator map showing polyhydrated sulfates in light blue and monohydrated sulfates in yellow-green, (c) mineral indicator map showing olivine in red, low-Ca pyroxene in green, and high-Ca pyroxene in blue.

outcrops for parts of mounds A and B. Hydrated sulfate components are highlighted in Figure 4b by using parameters that feature monohydrated sulfates in light green in mounds A and B, plus PHS in light blue in mound B. The mafic components are highlighted by using different spectral parameters in Figure 4c and include low-Ca pyroxene (dark green) and olivine (red) in the southwest wall rock, as well as outcrops of high-Ca pyroxene (dark blue) and olivine (red) in the northeast wall rock. Most of the wall rock is covered by at least a thin layer of dust or sand, as suggested earlier for the Valles Marineris region [*Lucchitta et al.*, 1992; *McEwen et al.*, 1999], that obscures the mafic spectral signatures of the bedrock. Most of the chasma is filled with basaltic sand as observed in Figure 3 and described in previous studies [*Chapman et al.*, 2003; *Catling et al.*, 2006], although one green patch of low-Ca pyroxene is observed on the chasma floor (Figure 4c).

[20] CRISM targeted images provide more detailed information on composition and stratigraphy of the sulfate and mafic components. Selected images are shown in Figure 5 to illustrate the sulfate exposures in mounds A–D. Paired images are provided for each mound: a false color IR image for more accurate representation of the surface features and a sulfate map created from band depths near 1.9 μm indicative of water in most minerals (BD1900), a band depth near 2.1 μm indicative of water in monohydrated sulfates (BD2100), and a drop in reflectance near 2.4 μm that is characteristic of many sulfates (SINDEX, see Table 1 for parameter formulae). Monohydrated sulfates are displayed here in yellow and PHS in blue. The monohydrated sulfates are identified in CRISM spectra by the presence of two absorption bands near 2.1 and 2.4 μm. PHS spectra are identified by a band near 1.96 μm and a drop in reflectance near 2.4 μm. Monohydrated sulfates are found in each of the mounds, but the areal occurrence of PHS varies greatly. Mound B exhibits a large outcrop of material spectrally dominated by PHS, whereas mounds A and C contains PHS only in smaller abundances mixed with the monohydrated sulfate.

[21] We did not find any evidence for gypsum ($CaSO_4 \cdot 2H_2O$) in any of the mounds as originally suggested by *Gendrin et al.* [2005] in analyses of OMEGA spectra. The absence of gypsum in CRISM images is consistent with another recent study of OMEGA data of the Juventae Chasma region that found no gypsum [*Kuzmin et al.*, 2009]. *Kuzmin et al.* [2009] also performed thermodynamic modeling of sulfates including gypsum that suggest it is not present here. Previous analyses of ILD formation [e.g., *Catling et al.*, 2006] may need to be reconsidered given the absence of gypsum in the mounds.

4.2. Spectral Characterization of Sulfate Minerals in the Mounds

[22] CRISM I/F spectra are shown in Figure 6 along with lab spectra of selected sulfate minerals in order to illustrate the spectral properties of the sulfate minerals observed in mounds A–C at Juventae Chasma. The most common hydrated sulfates contain multiple water molecules in their unit cell structures and are termed polyhydrated sulfates (PHS). The monohydrated sulfates have only one H_2O per unit cell and are typically observed with either Fe or Mg in

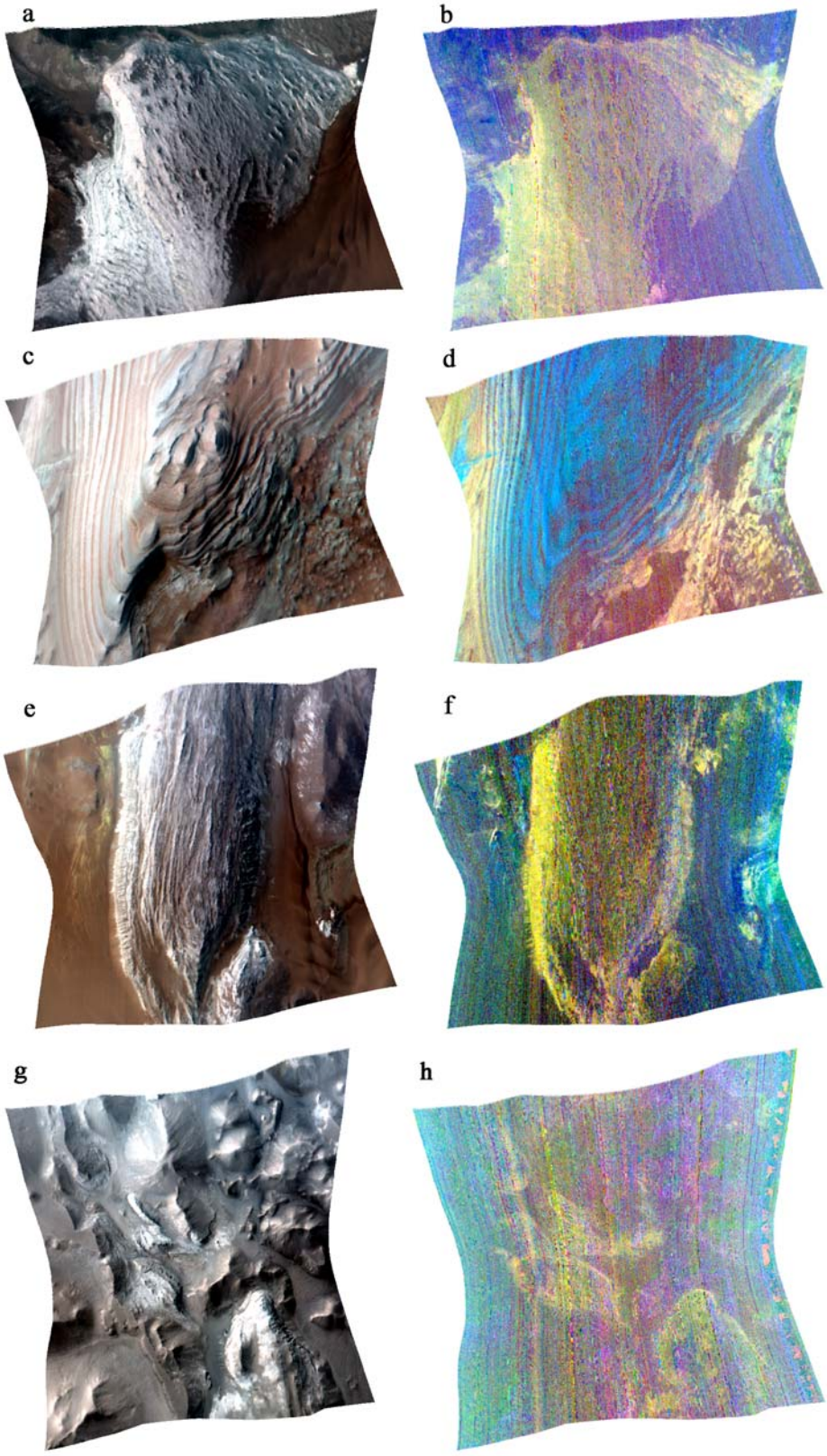

Figure 5. CRISM images of portions of the light-toned layered mounds: (a–b) mound A in image FRT00005C2B, (c–d) mound B in image FRT00009C0A, (e–f) mound C in image FRT000097A8, and (g–h) mound D in image FRT0000A4CF. The false color IR images (Figures 5a, 5c, 5e, and 5g) are mapped with R at 2.5 μm, G at 1.5 μm, and B at 1.1 μm, and the mineral indicator maps (Figures 5b, 5 d, 5f, and 5h) show polyhydrated sulfates in blue (BD1900) and monohydrated sulfates in yellow (BD2100+SINDEX).

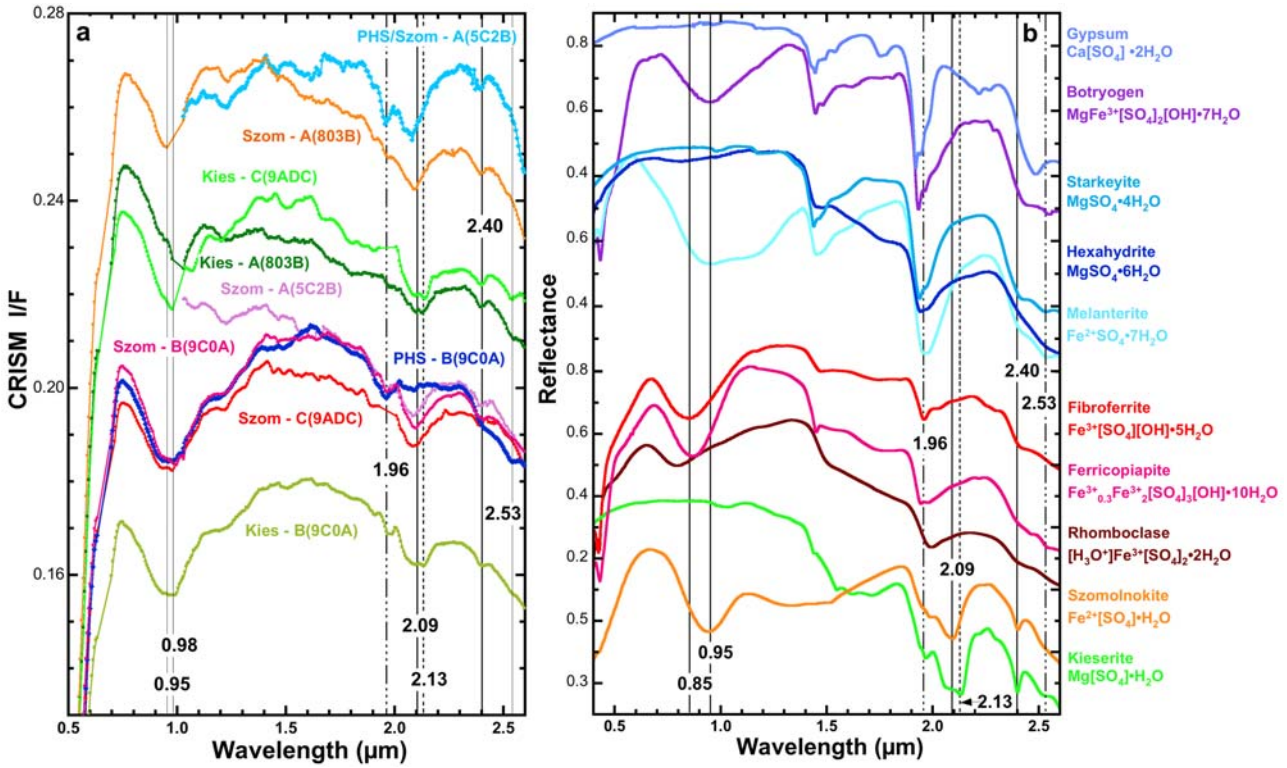

Figure 6. Reflectance spectra of polyhydrated and monohydrated sulfate spectra: (a) CRISM data from mounds A, B, and C, where PHS indicates PHS (blue colors), Szom indicates szomolnokite (red/orange/pink colors), and Kies indicates kieserite (green colors) and the image number is given following the mound ID, and (b) lab spectra of selected polyhydrated and monohydrated sulfates for comparison.

the cation sites. Summaries of the structures and spectral properties of sulfate minerals have been published recently [*Hawthorne et al.*, 2000; *Crowley et al.*, 2003; *Cloutis et al.*, 2006; *Lane et al.*, 2008]. In this study we have focused on the near-infrared bands in the 1.7–2.6 μm range that are due to combination and overtone bands of H_2O, OH, and SO_4, as summarized by *Bishop and Murad* [2005] for jarosite group minerals. The H_2O stretch-plus-bend combination band normally occurs between 1.92 and 1.98 μm for PHS and 2.08–2.13 μm for monohydrated sulfates; the vibrational energy varies slightly depending on the proximity of SO_4 groups, metal cations and other H_2O molecules that influence the charge distribution on the bound water molecule in the mineral structure and the degree of H bonding. Monohydrated sulfates also exhibit a narrow band at 2.40 μm. Many PHS spectra have weak bands or shoulder features between 2.40 and 2.55 μm. These are attributed to combinations and overtones of SO_4 and H_2O groups. Weak OH stretch-plus-bend combination bands can be observed near 2.25–2.3 μm for fibroferrite, ferricopiapite, botryogen, and gypsum. Kieserite spectra also have a broad absorption band from ~1.55–1.75 μm and gypsum spectra exhibit a band near 1.75 μm.

[23] One of the best examples of PHS spectra at Juventae Chasma is found in a smooth outcrop at the top of mound B, which is plotted in dark blue in Figure 6a and labeled PHS-B(9C0A). This spectrum includes a strong water combination band near 1.96 μm and a reflectance drop with two minima near 2.40 and 2.53 μm. These features can be compared to the lab spectra of hydrated sulfates in Figure 6b. Many hydrated sulfate minerals exhibit features near 1.96, 2.4 and 2.53 μm and the spectra of botryogen ($MgFe^{3+}(SO_4)_2(OH)\cdot 7H_2O$), starkeyite ($MgSO_4\cdot 4H_2O$), hexahydrite ($MgSO_4\cdot 6H_2O$), melanterite ($Fe^{2+}SO_4\cdot 7H_2O$), fibroferrite ($Fe^{3+}(SO_4)(OH)\cdot 5H_2O$), ferricopiapite ($Fe^{3+}_{0.3}Fe^{3+}_2(SO_4)_2(OH)\cdot 10H_2O$), and rhomboclase ($((H_3O^+)Fe^{3+}(SO_4)_2\cdot 2H_2O$) are all possible matches; however, the spectra of starkeyite, melanterite, and ferricopiapite are the most consistent with the PHS spectra observed for the mound B outcrops. At this point we are unable to make a unique mineral assignment to the PHS spectra observed at Juventae Chasma.

[24] Monohydrated spectral signatures are observed nearly everywhere across mounds A–D and are identified by bands centered near 2.1 and 2.4 μm and the absence of the 1.9 μm water band. The shape of the water band near 2.1 μm differs for szomolnokite ($Fe^{2+}SO_4\cdot H_2O$) and kieserite ($MgSO_4\cdot H_2O$), thus enabling detection of these specific minerals. The spectrum of natural szomolnokite is characterized by a fairly symmetric band centered at 2.09 μm, while the spectrum of natural kieserite is characterized by an asymmetrically shaped band with a reflectance minimum at 2.13 μm (Figure 6b). The szomolnokite spectrum also has an Fe^{2+} electronic transition absorption band at 0.95 μm and the kieserite spectrum contains a strong broad band from ~1.55–1.75 μm. Some synthetic kieserites exhibit a more symmetrically shaped band centered near 2.11 μm (R. Milliken, unpublished data, 2008) that would be more difficult to distinguish from szomolnokite spectra.

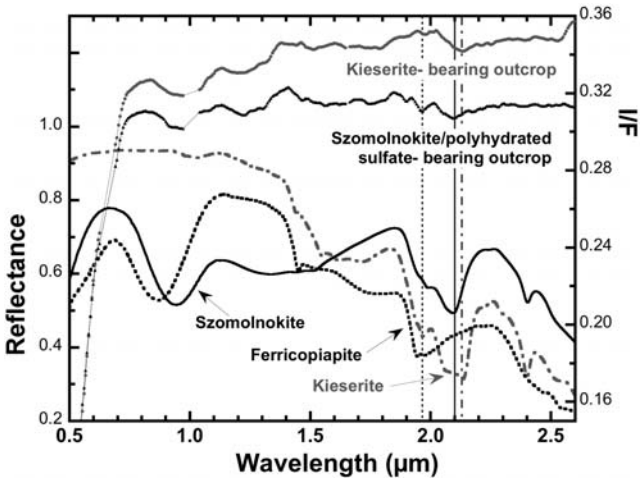

Figure 7. CRISM spectra of hydrated spectra from mound D compared with lab spectra. The lines mark features at 1.98, 2.09, and 2.13 μm.

[25] Spectra of the ILD deposits at mound D (Figure 7) are brighter in general than spectra of mounds A–C (0.31–0.36 reflectance at mound D versus 0.18–0.28 for mounds A–C), and exhibit weaker sulfate bands. A band near 2.13 μm is observed in spectra attributed to kieserite-bearing rocks and bands near 1.96 and 2.09 μm are observed in spectra of rocks containing both szomolnokite and another hydrated component (likely PHS). It is difficult to clearly resolve a band at 2.4 μm in the mound D spectra as is observed in spectra of the ILDs on mounds A–C.

[26] As the CRISM spectra are not ratioed, the relative brightness of the different minerals in each mound can also be compared. In general, the kieserite-bearing units in mounds A and B tended to have darker spectra than the szomolnokite-bearing units; compare for example Kies-A(803B) to Szom-A(803B) and Kies-B(9C0A) to Szom-B(9C0A) in Figure 6a. This indicates that the kieserite units are likely mixed with a darker material. The reverse trend was observed for mounds C (Figure 6a) and D (Figure 7). In addition to mixing with darker sand/dust, surface texture and illumination could be contributing to the relative brightness of these spectra. *Catling et al.* [2006] found thermal inertia to be well correlated with visible albedo for the mounds. A high thermal inertia, indicative of a rocky surface, is observed at mound A, which is the brightest in visible albedo. For mounds B and C, *Catling et al.* [2006] found higher thermal inertias along the brighter edge regions than on top of the mounds, which they attribute to dust/sand coating the upper portions of these mounds. This is consistent with our spectral observations of stronger sulfate signatures at lower elevations, especially for mound C.

[27] Most of the sulfate-bearing spectra on the mounds have an Fe band centered near 0.95 μm that is consistent with szomolnokite. This could mean that szomolnokite is present everywhere at different abundances and is spectrally dominant near 1 μm, but not near 2 μm. Another explanation is that a separate Fe phase is present in the dust that is covering and/or intermixed with the sulfate rocks on the mounds. Experiments testing the influence of fine-grained iron oxide–bearing particles coating a rock surface were performed recently in order to help understand CRISM spectra [*Parente et al.*, 2008]. Spectral analyses of these coated rocks indicate that only a few particles sprinkled on the surface are sufficient to alter the spectral properties of the rock in the visible region, while having only a minor effect on the NIR bands from 1.9 to 2.5 μm.

4.3. Stratigraphy of Sulfate Minerals in the Mounds

[28] The abundances of kieserite and szomolnokite were mapped as a function of elevation in order to gain more insight into the relative positions of these monohydrated sulfate minerals. PHS were not included in the elevation study because they are absent (or present only as mixtures in a few smaller locations) except in mound B. The mean elevation of the monohydrated sulfates kieserite and szomolnokite is plotted in Figure 8 for mounds A, B, and C. The plot indicates that the kieserite layer is typically found at higher elevation than the szomolnokite in mound C. The results are more ambiguous for mounds A and B; however, the mean kieserite elevation is higher than the mean szomolnokite elevation for both mounds. Inspection of HiRISE and CTX images of these mounds and comparison of the spatial distribution of these minerals suggests that the kieserite layer drapes the szomolnokite unit. These analyses indicate that szomolnokite appears at higher elevations in some cases in the current views of the mounds where erosion has created a window through the kieserite to the szomolnokite below. This indicates that szomolnokite was deposited first, followed by kieserite, and that the stratigraphic relations for all three mounds were similar. However, the absolute elevations of the layers are not consistent among the mounds. The elevations of the sulfate layers in mound C are significantly lower than those in mounds A and B. This suggests that either mound C was formed independently from mounds A and B, or that the ground on which mound C now sits subsided relative to the ground on which mounds A and B sit.

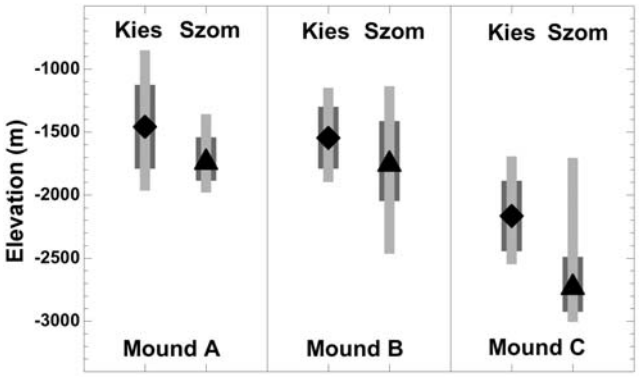

Figure 8. Stratigraphy of monohydrated sulfates in mounds A, B, and C, where Kies refers to kieserite and Szom refers to szomolnokite. Elevation is shown in meters for each sulfate mineral in images FRT00005C2B and FRT0000803B for mound A, images FRT00005633 and FRT00009C0A for mound B, and images FRT00009ADC and FRT000097A8 for mound C. The mean is plotted along with two sets of error bars for each image investigated: the first error bars are standard deviations and the second sets are minimum and maximum values.

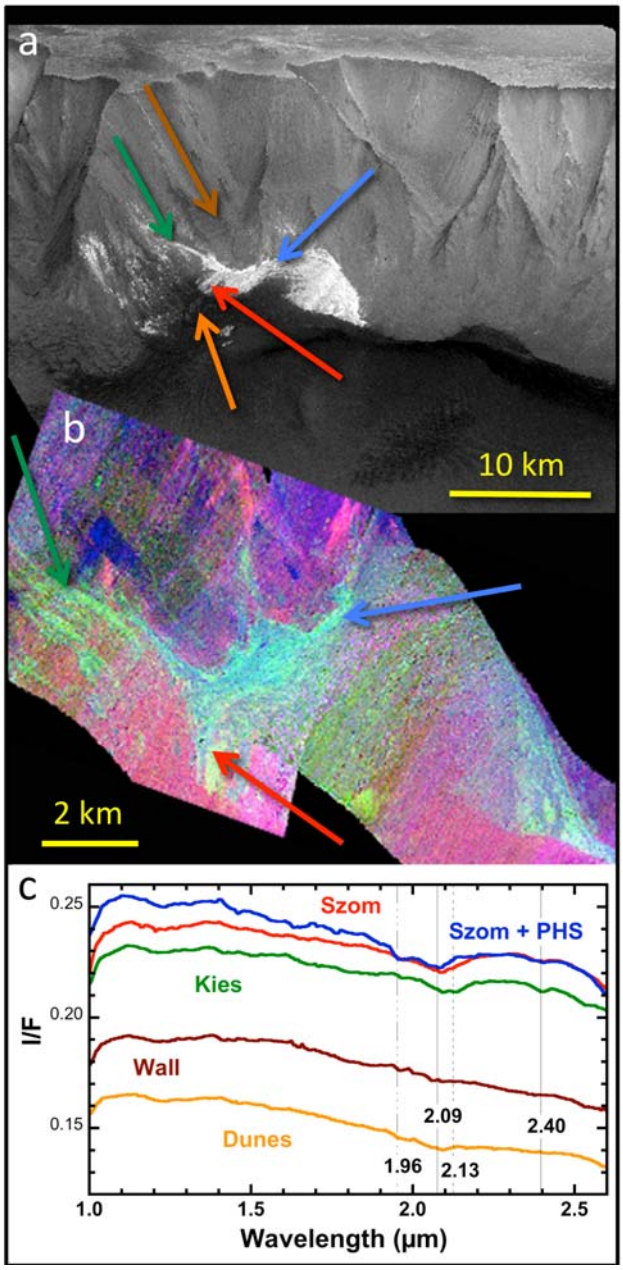

Figure 9. Composition of mound A: (a) HRSC image H0243_0000 (prepared for Figure 3b) showing mound A exposed from the wall rock. (b) CRISM mineral indicator mosaic (images FRT0000803B and FRT00005C2B) draped over an HRSC DEM showing kieserite in green, szomolnokite plus polyhydrated sulfate in blue, and in pink nonsulfate material purple tones. (c) CRISM spectra from FRT0000803B showing relative albedos of the brightest material containing szomolnokite (Szom), a slightly darker kieserite-bearing unit (Kies), and the much darker wall rock (Wall) and dune (Dunes) material. Colored arrows on Figures 9a and 9b correspond to the colors of the spectra shown in Figure 9c.

4.4. Morphology and Stratigraphy of ILD Material at Mound A

[29] A low-angle HRSC view of mound A is presented in Figure 9a in order to more clearly show the bright sulfate-bearing ILD along the chasma wall. The topography of mound A is shown in a CRISM mosaic of mineral indicator maps overlain on an HRSC DEM in Figure 9b. Figure 9c shows spectra of selected ILD spots at mound A compared to the darker wall rock and dune spectra. The five spectra were retrieved as end-members from CRISM image FRT0000803B using a pixel purity index (available in ENVI's spectral analysis package). The kieserite, szomolnokite, and szomolnokite plus PHS end-members were used to generate the mineral parameter map in Figure 9b, where the region spectrally dominated by kieserite is mapped in green on the western portion of mound A and the szomolnokite/PHS units are mapped in blue/purple.

[30] The morphology and texture of the ILD material at mound A can be seen in the HiRISE views shown in Figure 10. The western region of the mound that is spectrally dominated by kieserite shows linear bedding features (Figure 10b), while the central region dominated by szomolnokite spectral features exhibits a different, massive texture (Figure 10c). The kieserite unit observed in Figure 10b shows the layers to be a combination of light and dark material that would be mixed at the CRISM resolution of 18 m/pixel. This could explain the lower I/F values for the kieserite-bearing unit in mound A compared to the szomolnokite-rich material. HiRISE false color images show texture and color differences between the side of the mound (Figures 10d and 10e) and the top of the mound (Figures 10b and 10c). The material at the top is whitish/gray with a smooth and rounded morphology, while the side of the mound at this location is brown and has a blocky morphology. The eastern tip of the mound, where the highest concentration of PHS is observed, is shown in Figure 10f. Spectra of this material exhibit the strongest band near 1.96 μm for mound A (PHS/Szom spectrum in Figure 6a).

4.5. Morphology and Stratigraphy of ILD Material at Mound B

[31] Mound B is larger than mound A and emerges from the chasma floor as seen in Figures 11–12. The CTX anaglyph (Figure 12a) shows that bright material extends away from the mound on the eastern side suggesting that this mound was once larger and that a sizable section on the eastern side has been eroded away. Alternatively, this could be a fan of erosive debris.

[32] The approximate locations of the three spectrally distinct components of ILD material at mound B are shown in Figure 11b. Spectra consistent with PHS (Figure 11a) are found at the top of the mound and are mapped in purple in Figure 11b. Spectra dominated by kieserite signatures (Figure 11c) are mapped in yellow-green in the sheltered alcove eroded out of the central front section of the mound and downslope from that toward the southeast (Figure 11b). The szomolnokite-bearing spectra (Figure 11c) are found downslope from the PHS-bearing material along the west and northeast flanks of the mound (Figure 11b). A mixture spectrum was collected part way down the west side of the mound that shares the spectral properties of both PHS and szomolnokite (Figure 11a, spectrum 3). The CRISM spectra

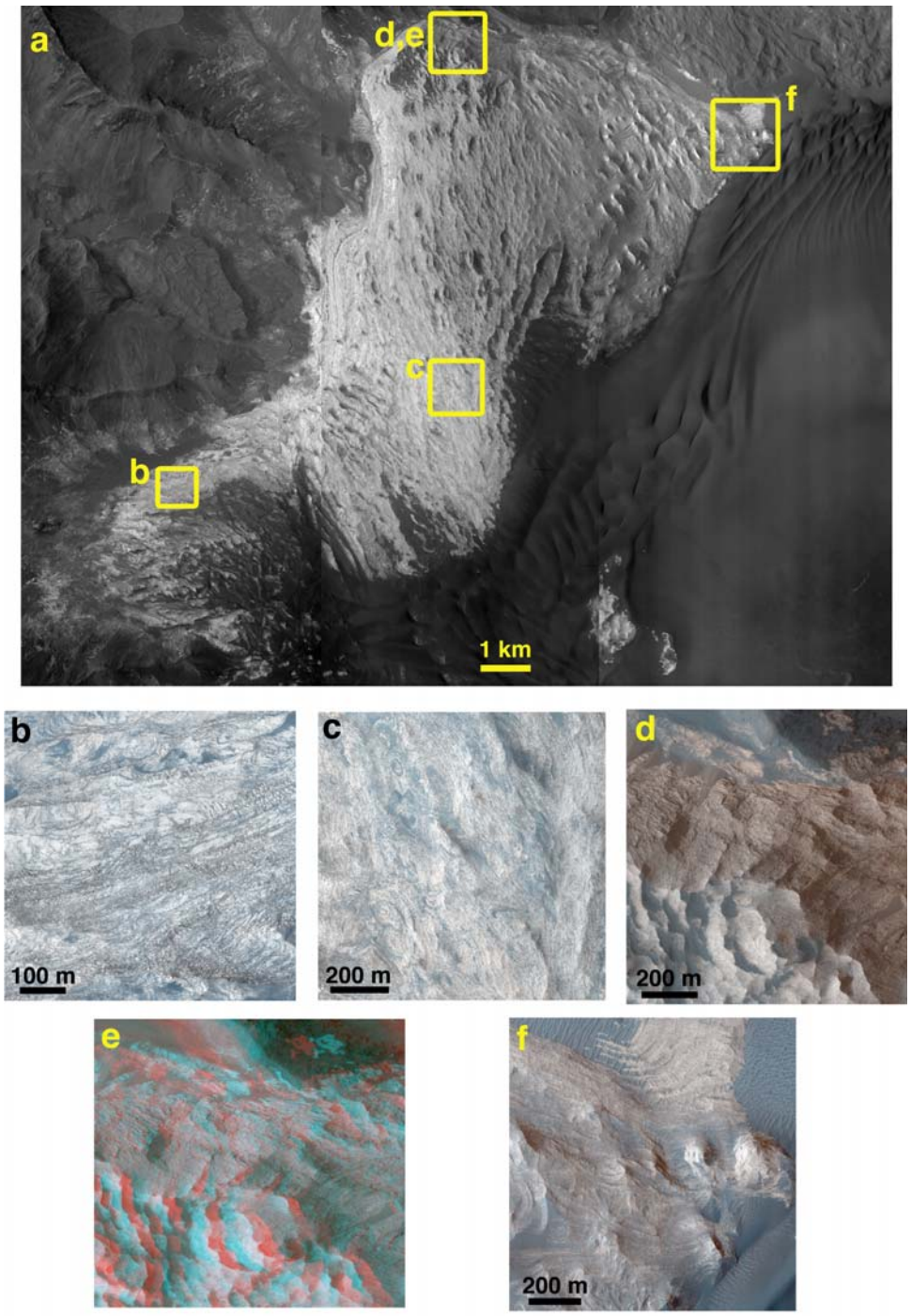

Figure 10. (a) HiRISE mosaic (images PSP_004291_1755 and PSP_005557_1755) of mound A region. (b) Views of regions dominated by kieserite. (c) Views of regions dominated by szomolnokite. (d) HiRISE color shows that the top of the mound is whitish/gray, but the sides of the mound are brown. (e) A stereo anaglyph of the side of the mound. (f) A view of the eastern tip of the mound with the highest PHS abundance.

of mound B in Figure 11 also highlight the changes in brightness of the three types of sulfate units present here: the PHS-bearing rocks are the brightest, followed by the szomolnokite-bearing layer and the kieserite-bearing unit is the darkest.

[33] Evaluation of the visible/near-infrared data show evidence of hematite mixed with the szomolnokite bedrock of mound B. Shown in Figure 11d are spectra of a szomolnokite-dominated unit (region 9), a nearby spectrally neutral patch (region 10), PHS-dominated material at higher elevation on the mound (region 11) and a spectrally neutral region nearby (region 12). Ratio spectra for the szomolnokite-bearing rocks versus the PHS-bearing rocks show a pronounced difference in character from $\sim$0.8–1 μm. A recent

study has used this technique for analysis of ferric oxide components in some sulfate layers in the Valles Marineris region (L. H. Roach et al., Diagenetic hematite and sulfate assemblages in Valles Marineris, submitted to *Icarus*, 2009). A ratioed and continuum removed spectrum of the szomolnokite-bearing rocks shows a band centered near 0.87 μm that is consistent with hematite [*Morris et al.*, 1985], although it is difficult to uniquely identify specific iron minerals in mixtures using this technique. What this does show is that an iron-containing mineral (likely ferric oxide/hydroxide or sulfate) is present in the szomolnokite-rich rocks that is not present in the PHS-rich rocks.

[34] Figure 12 shows close-up views of the layering and different textures observed at mound B. The PHS-bearing material at the top of mound B is shown in Figures 12c and 12d. Figure 12c is a HiRISE view of the smooth material near the top of the mound containing the strongest PHS signature. Figure 12d shows the bright polyhydrated layers that are partially covered by darker debris. At lower elevations on the mound these layers exhibit spectral features of both szomolnokite and PHS, so the darker material in these layers toward the base of the mound may contain szomolnokite. Figure 12e highlights a distinct dark layer present near the top of the mound. This material likely eroded into smaller grains that subsequently shed downslope to collect as dark debris bands on top of the brighter PHS-bearing layers as shown in Figure 12d. Kieserite-bearing outcrops can be seen in Figures 12f and 12g that correspond to spectra collected at spots 7 and 8 in Figure 11c. The surface in Figure 12f appears altered and eroded and shows some layers that are partly covered by sand or dust. The material shown in Figure 12g appears rather smooth and featureless, although it has similar spectral properties to the layered material shown in Figure 12f. Possibly, the region shown in Figure 12f exhibits more layering because it is on a steep slope where wind erosion has better exposed the layering. The region shown in Figure 12g is located on a more horizontal area that could have experienced less wind erosion and/or that could have collected kieserite-bearing debris from the slopes above it. The szomolnokite-bearing outcrops for mound B have not yet been covered by HiRISE.

4.6. Morphology and Stratigraphy of ILD Material at Mound C

[35] Mound C is the largest of the sulfate mounds at Juventae (Figure 2) and is located northeast of mound B. A HiRISE anaglyph of the southern part of the mound is displayed in Figure 13a and shows steep slopes at the sides of the mound and multiple smaller light-toned outcrops adjacent to the mound. HiRISE views of two monohydrated sulfate outcrops on mound C are shown in Figures 13b and 13c. These illustrate the fine-scale layering and mixed bright/dark material. Figure 13d is a CRISM image of the southern

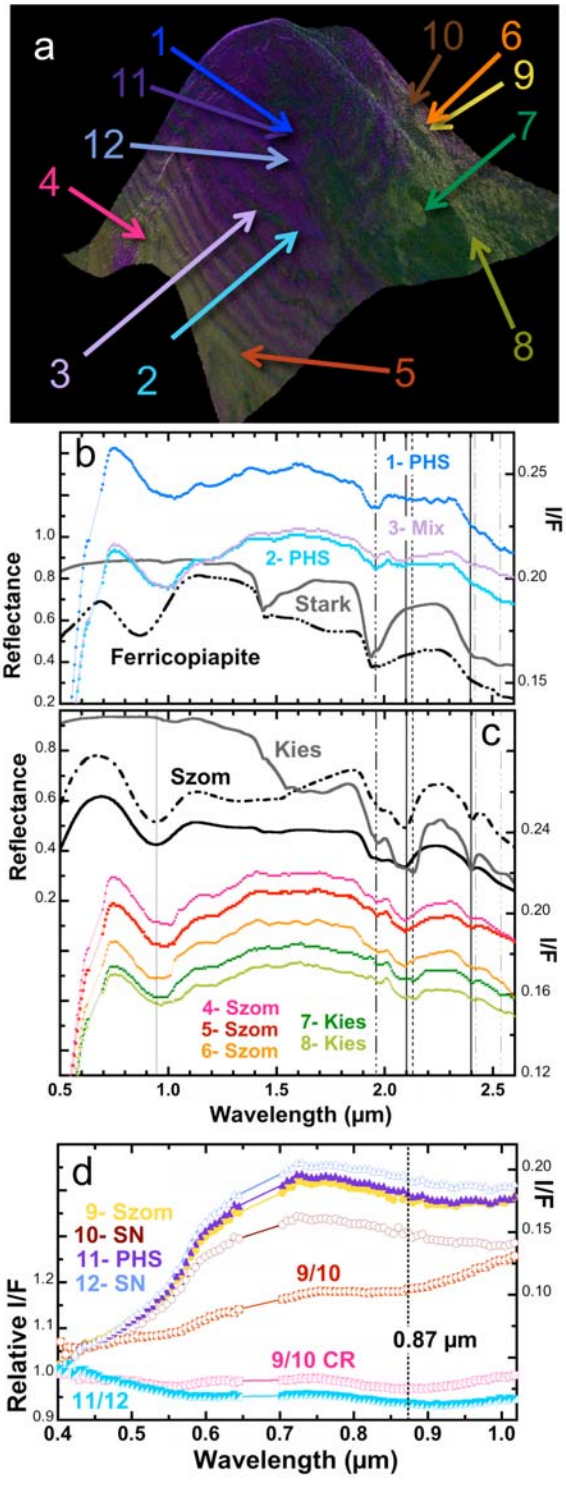

Figure 11. Composition of mound B determined through analysis of CRISM image FRT00009C0A: (a) map of CRISM image FRT00009C0A draped over HRSC topography with PHS mapped in purple, szomolnokite mapped in yellow, and kieserite mapped in green, (b) spectra collected from two 20 × 20 regions characteristic of PHS and one 20 × 20 mixture (Mix) region that contains spectral features due to PHS and szomolnokite, (c) spectra collected from 20 × 20 regions of three szomolnokite (Szom)-bearing regions and two kieserite (Kies)-bearing regions; lines are present at 0.95, 1.96, 2.09, 2.13, and 2.40 μm, and (d) 0.4–1.0 μm spectra collected from ROIs of szomolnokite (Szom)- and PHS-bearing regions and spectrally neutral (SN) patches nearby, ratios of these spectra, and a continuum removed (CR) spectrum of the Szomolnokite ratio spectrum.

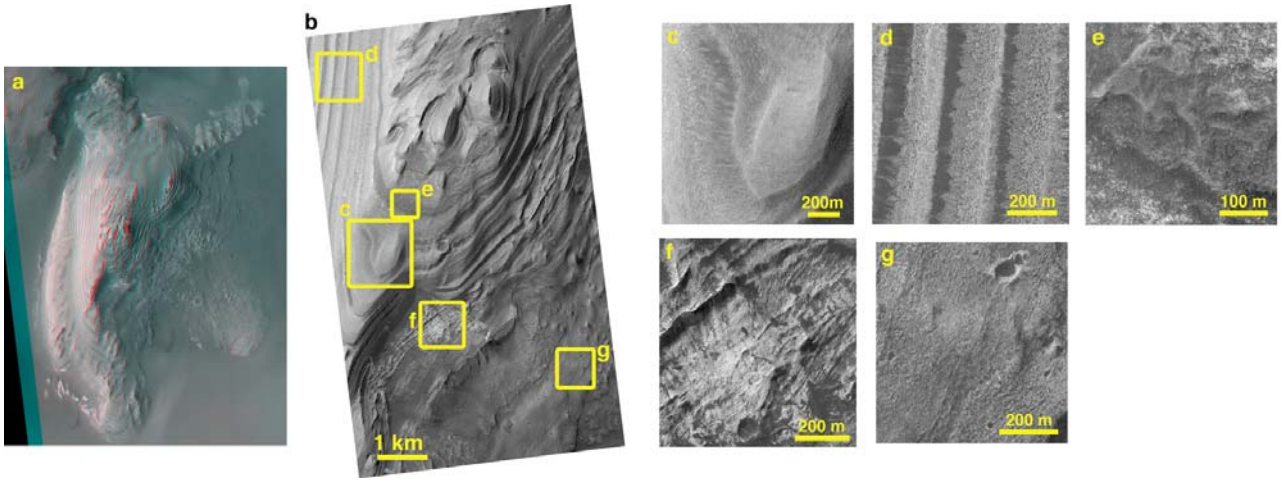

Figure 12. Textures of mound B: (a) CTX anaglyph, (b) HiRISE image PSP_007126_1755 with boxes for the locations of expanded views, (c) bright region showing the highest concentration of polyhydrated sulfate (Figure 11c, spectrum 1), (d) view of terraced slopes where bright polyhydrated material is partly covered by bands of dark debris that is obscuring the underlying sulfate deposit. This may be due to topography concentrating the dark debris in relative topographic lows between bedding. (e) Dark layer ~200 m across that probably eroded into smaller grains and shed downslope where it collected to form the dark debris banding units on top of the brighter polyhydrated sulfates seen in Figure 12d, (f) kieserite layers in a sheltered alcove under steep slopes of bright material containing polyhydrated sulfate (Figure 11c, spectrum 7), and (g) darker kieserite-bearing outcrop downslope (Figure 11c, spectrum 8).

part of the mound showing the light-toned sulfate outcrops and brown colored dust/sand at the base of the mound and coating parts of the ILD material. CRISM spectra of five spots in this image are shown in Figure 13e that are representative of the szomolnokite- and kieserite-bearing units. The strongest szomolnokite signatures (band centers at 2.09 and 2.40 μm) are found in the lower portions of the mound on the eastern side. The strongest kieserite features (band centers at 2.13 and 2.40 μm) are found at higher elevations on the western side of the mound. Spectrum 3 in Figure 13e is characteristic of both kieserite and szomolnokite and likely includes both of these minerals. Multiple textures are observed for this region (Figure 13b) which is consistent with parts of the kieserite layer being eroded away to show szomolnokite below. All of the spectra shown in Figure 13e also have a feature near 1.96 μm attributed to PHS. This could be material from the higher PHS unit that has come loose and covered the monohydrated sulfates or it could be due to partial hydration of the monohydrated sulfate rocks.

4.7. Spectral Characterization of Mafic Minerals at Juventae Chasma

[36] Small outcrops of mafic rocks were observed at the base of mound C in CRISM image HRL0000444C. These are rare occurrences as most of the chasma floor is covered by basaltic sand. We used regions of interest (ROIs) to isolate spectra dominated by olivine and pyroxene in the bedrock that are mapped in pink and blue, respectively, at the top of Figure 14a. Parente et al. (submitted manuscript, 2009) selected another ROI of spectrally neutral material in order to generate ratio spectra of the olivine-rich and pyroxene-rich outcrops. These ratio spectra are shown in Figure 14b along with lab reflectance spectra of olivine in Chassigny and orthopyroxene in ALH 84001. Gaussian modeling of the olivine spectrum gives primary bands centered at 0.86, 1.07, and 1.22 μm (Parente et al., submitted manuscript, 2009) that are consistent with a fayalitic olivine [*Sunshine and Pieters*, 1998]. Comparing this spectrum with that of Chassigny (Fo68) [*Mason et al.*, 1975] implies a more iron-rich composition for the olivine at Juventae than observed in this Martian meteorite as the band centers occur at slightly longer wavelengths [*Sunshine and Pieters*, 1998]. Gaussian modeling of the Juventae pyroxene spectrum gives two absorptions in the 1-μm region centered at 0.91 and 1.05 μm (Parente et al., submitted manuscript, 2009) that are consistent with orthopyroxene [*Sunshine and Pieters*, 1993] and similar to the bands resulting from fits of spectra of the orthopyroxene-bearing meteorite ALH 84001 (Parente et al., submitted manuscript, 2009).

[37] One set of olivine-rich and pyroxene-rich outcrops from CRISM image HRL0000444C is featured in HiRISE image PSP_002946_1765 in Figure 15. A HiRISE stereo anaglyph (Figure 15a) illustrates the topography of the northern part of mound C. Distinct units are marked in Figure 15b for the olivine- and pyroxene-rich rocks.

[38] The spectral character of the mafic minerals observed in the small outcrops near mound C are similar to those of the large outcrops (several km across) in the bedrock exposed along the southwest and eastern walls of the chasma. Distinct outcrops of material dominated by low-Ca pyroxene, high-Ca pyroxene, or olivine have been found and comprise about 10% of the wall rock observed to date. The remaining 90% of the wall rock does not exhibit strong features characteristic of one of these minerals, but could be dominated by plagioclase that is not readily detected using VNIR spectra. As shown in Figure 3, dust covers much of the wall rock as noted previously in chasma of the extended Valles

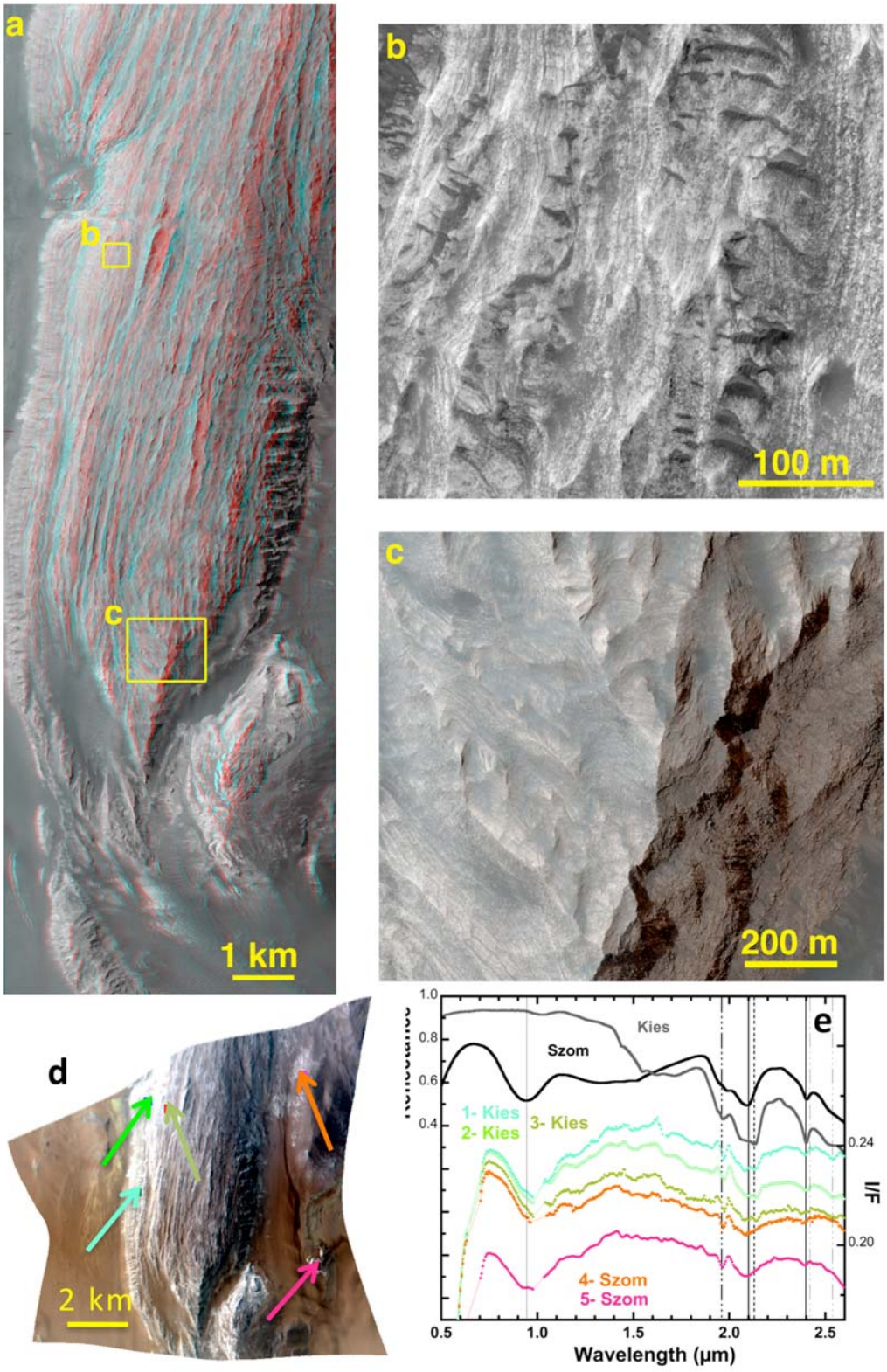

Figure 13. Textures of mound C from HiRISE image PSP_006915_1760: (a) a portion of the HiRISE stereo anaglyph for the southern portion of the mound, (b) a view of material that shows spectra consistent with a mixture of szomolnokite and kieserite, (c) a false color blowup along the southern tip of the mound where the shallower surface along the western edge appears whitish/gray whereas the steeper eastern edge appears brown, (d) CRISM image FRT00009ADC with R at 2.5 μm, G at 1.5 μm, and B at 1.1 μm with arrows corresponding to the spectra of (e) kieserite-rich and szomolnokite-rich regions; lines are present at 0.95, 1.96, 2.09, 2.13, and 2.40 μm.

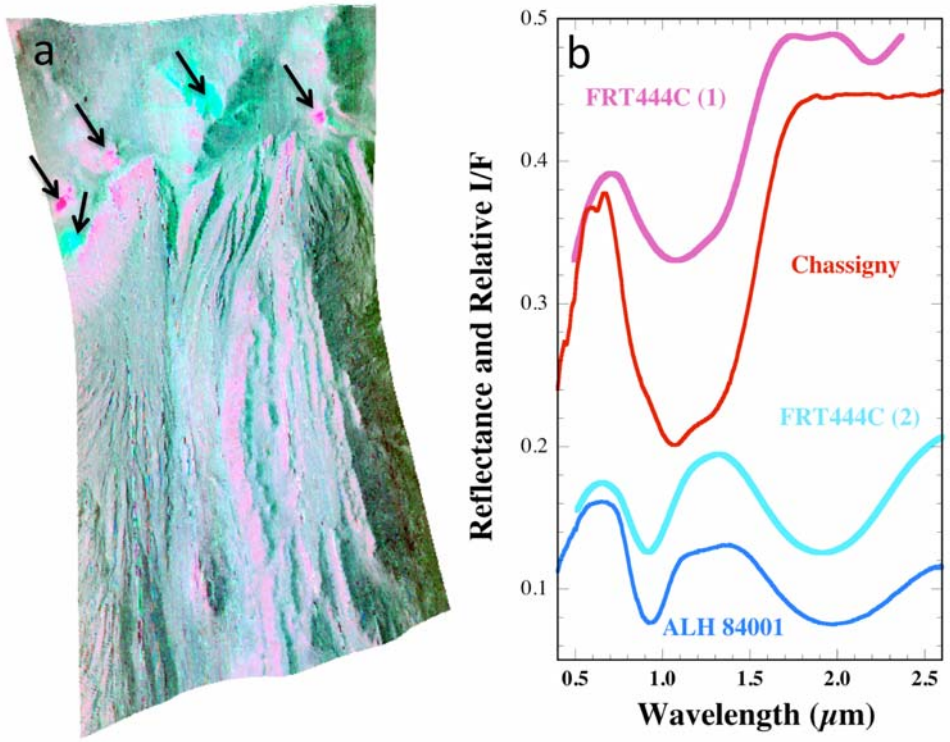

Figure 14. Olivine and pyroxene collected in bedrock near mound C. (a) CRISM image HRL0000444C with pink olivine and blue pyroxene outcrops marked by arrows (note that pink tones on top of the mound are due to Fe^{2+} in the sulfate and not to olivine), (b) CRISM spectra from this image of (1) olivine- and (2) pyroxene-bearing regions compared to lab spectra of meteorites. The CRISM spectra are ratios of regions of interest spectrally dominated by olivine or pyroxene divided by spectrally unremarkable regions (Parente et al., submitted manuscript, 2009). The ALH 84001 orthopyroxene spectrum is from *Bishop et al.* [1998], and the Chassigny olivine spectrum is from D. Dyar (unpublished data, 2008).

Marineris region [*Lucchitta et al.*, 1992; *McEwen et al.*, 1999]; thus, dust likely obscures the spectral features at Juventae of the largely mafic bedrock below.

4.8. Spectral Characterization of Aqueous Minerals on the Plateau

[39] The plateau region northwest of Juventae Chasma includes several LLD components [*Mangold et al.*, 2008; *Weitz et al.*, 2009]. One of these is featured in Figure 16. The sinuous lineations observed in light blue in the CRISM false color image (Figure 16a) are mapped as two separate components (gold and magenta) in Figure 16b using spectral features near 2.2 μm (see Table 1). Relative CRISM I/F spectra were created by selecting long thin ROIs of the gold and magenta areas and ratioing these to a spectrally unremarkable ROI from the same image. These are shown in Figure 17 and are two of the many beds observed in the LLD on the plateau west of Juventae Chasma [*Mangold et al.*, 2008; *Weitz et al.*, 2009]. We featured these two materials in this study because of their unique spectral character. Both of these units occur as thin, elongated forms typically ~20 m across and hundreds of meters long, so they are just at the detection limit of CRISM. Other regions of the LLD in this area include a variety of light-toned layered materials and are associated with inverted channels in some places [e.g., *Weitz et al.*, 2009]. The variety of aqueous features in this region is consistent with the occurrence of multiple aqueous events on the plateau.

4.8.1. LLD Containing Hydrated Silica

[40] The gold ring-type material from Figure 16b exhibits bands near 1.39, 1.92, and 2.21 μm and is plotted in gold in Figure 17. This material has been identified as opaline silica and occurs in other young deposits at Ius Chasma, Melas Chasma and Noctis Labyrinthus [*Milliken et al.*, 2008]. Fully dehydrated silica gel (only Si-OH groups) exhibits spectral bands at 1.37 and 2.20 μm [*Anderson and Wickersheim*, 1964]. Upon hydration these bands broaden toward longer wavelengths with additional H bonding [*Anderson and Wickersheim*, 1964] producing bands attributed to Si-OH near 1.39 and 2.21–2.26 μm and to H_2O near 1.9 μm in opaline silica samples from Yellowstone [*Bishop et al.*, 2004] and Kilauea [*Bishop et al.*, 2005]. Spectra of opaline silica on altered basalt glass also has features near 1.39, 1.92, and 2.21 μm (shoulder toward 2.26 μm), but opal-CT spectra show a band near 1.41 μm instead of 1.39 μm, a much stronger band near 1.9 μm, and a broader band from 2.21 to 2.26 μm [*Milliken et al.*, 2008]. This is consistent with the features observed for silica gel with low levels of hydration [*Anderson and Wickersheim*, 1964]. A CRISM spectrum resembling hydrated silica is plotted for comparison with altered volcanic ash from Kilauea and Haleakala that have large components of amorphous hydrated silica phases. The

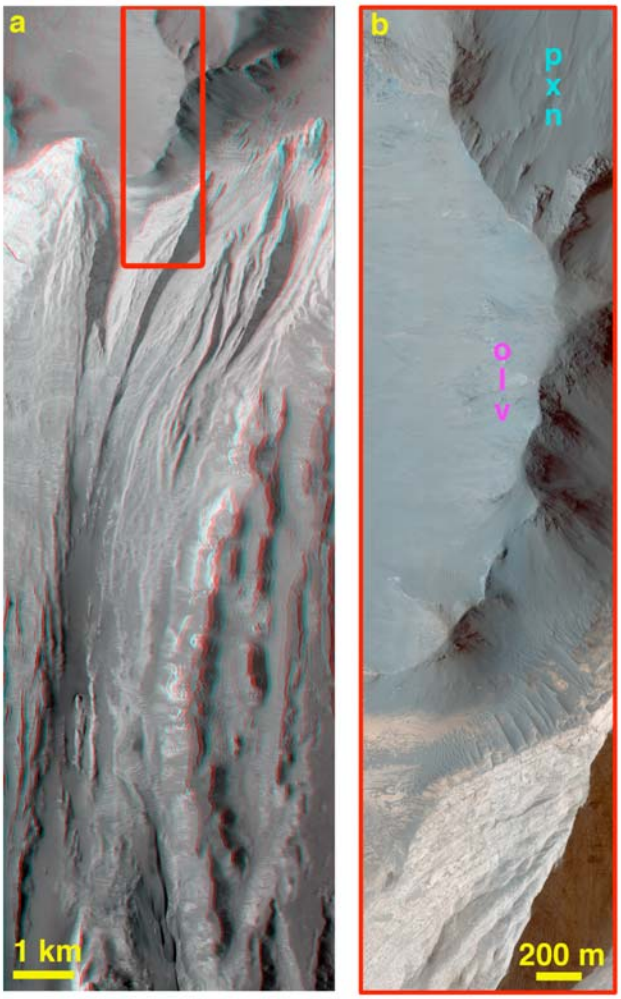

Figure 15. Mafic outcrops north of mound C: (a) HiRISE stereo anaglyph of the northern edge of mound C. (b) Portion of HiRISE false color image PSP_2946_1765 showing the northern tip of the ILD mound and wall rock spurs with bedrock exposures to the north. The pink olivine-rich and blue pyroxene-rich regions identified in CRISM spectra (Figure 14) are indicated here.

hydrated silica component in the plateau west of Juventae occurs at the geologic contact between the magenta material and the older plateau unit and has a broken and blocky texture shown in Figures 18c and 18e. Large cracks 5–10 m long are also present in this hydrated silica-bearing unit. This layer could either be the lowermost stratigraphy in the LLD or the uppermost surface of the plateau.

4.8.2. LLD Containing Hydroxylated Ferric Sulfate

[41] The magenta units in Figure 16b exhibit distinct spectral features, indicative of a different aqueous phase. Two examples of CRISM spectra of this material are shown in Figure 17. Spectrum a has a weak feature at 1.43 μm, followed by bands near 1.94 and 2.23 μm with approximately equal band strength, and another weak band at 2.40 μm. A similar spectrum, spectrum b, has a weak feature at 1.45 μm, a band at 1.95 μm that is roughly double the band depth of the feature at 2.23 μm, and a stronger band at 2.40 μm. Similar spectra were identified in this region by *Milliken et al.* [2008] as partially dehydrated sulfates.

[42] A narrow absorption band at 2.23 μm is fairly rare in geologic materials, but falls in the region expected for an OH combination band. Selected lab spectra are shown for comparison with the CRISM data in Figure 17. Jarosite spectra have a triplet feature due to Fe-OH with the strongest absorption at 2.27 μm and spectra of the phosphate mineral strunzite have a broad absorption near 2.23–2.25 μm due to Fe-OH. Alunite spectra (not shown) exhibit a band due to Al-OH near 2.17 μm [*Bishop and Murad*, 2005] and gypsum spectra (not shown) contain a doublet at 2.22 and 2.27 μm [*Bishop et al.*, 2004]. Copiapite and fibroferrite both have OH in their mineral structures and have weak shoulder features in the 2.2–2.3 μm range. Although some of these minerals exhibit a weak shoulder or reflectance drop off near 2.4 μm, none of these mineral spectra have a strong band at 2.40 μm as observed in some of the CRISM spectra of this magenta phase.

[43] Stepwise heating experiments to dehydrate copiapite showed formation of bands at 2.23 and 2.39 μm (Figure 17). The variations in the band depth and shape as a function of dehydration of this hydrated Fe sulfate mineral suggest that the spectral variations we see in the CRISM spectral properties of the magenta phase could be due to the presence of more than one similar ferric sulfate hydroxide ($Fe(SO_4)OH$) phase that could also be hydrated. CRISM spectra of the magenta phase also contain a broad H_2O band at 1.95 μm that could be due to water in the ferric sulfate hydroxide material or in another hydrated component. The partially dehydrated copiapite in our experiments contains a similar broad H_2O band at 1.95 μm. During our dehydration experiments (Figure 17) the copiapite sample became darker in the visible region (not shown) with heating at 200°C, but the sample was unstable and the 2.23 μm feature had disappeared when the sample was remeasured two weeks later. Dehydration studies performed on H_3O^+- jarosite [*Desborough et al.*, 2006] and szomolnokite [*Morris et al.*, 2009] also show the formation of a band near 2.23 μm. Thus, the band at 2.23 μm is attributed to Fe-OH sites in hydroxylated ferric sulfates and could have formed via multiple mechanisms.

[44] The magenta unit from Figure 16b has a highly stratified, terraced morphology shown in Figure 18. Multiple adjacent layers up to several meters thick [*Weitz et al.*, 2008] have eroded into swirling patterns with arcing ridges (Figure 18d). Individual beds extend over several kilometers in length and cross bedding has not been observed [*Weitz et al.*, 2008]. The ferric sulfate hydroxide unit appears fresher and smoother on the surface than the underlying hydrated silica unit. The light-toned beds of this finely layered deposit are interspersed with darker-toned beds of other materials. The HiRISE color variations of adjacent layers within the hydroxylated ferric sulfate unit (Figure 18d) and the slight variations in CRISM spectral signatures observed for this unit (Figure 17b) suggest that multiple related phases might be present. Larger outcrops of a related material with a band at 2.23 μm have also been identified at Aram Chaos; however the spectra of the ferric sulfate hydroxide material there have additional bands at 1.49 and 1.82 μm [*Lichtenberg et al.*, 2009] not observed in our spectra. Small outcrops of jarosite

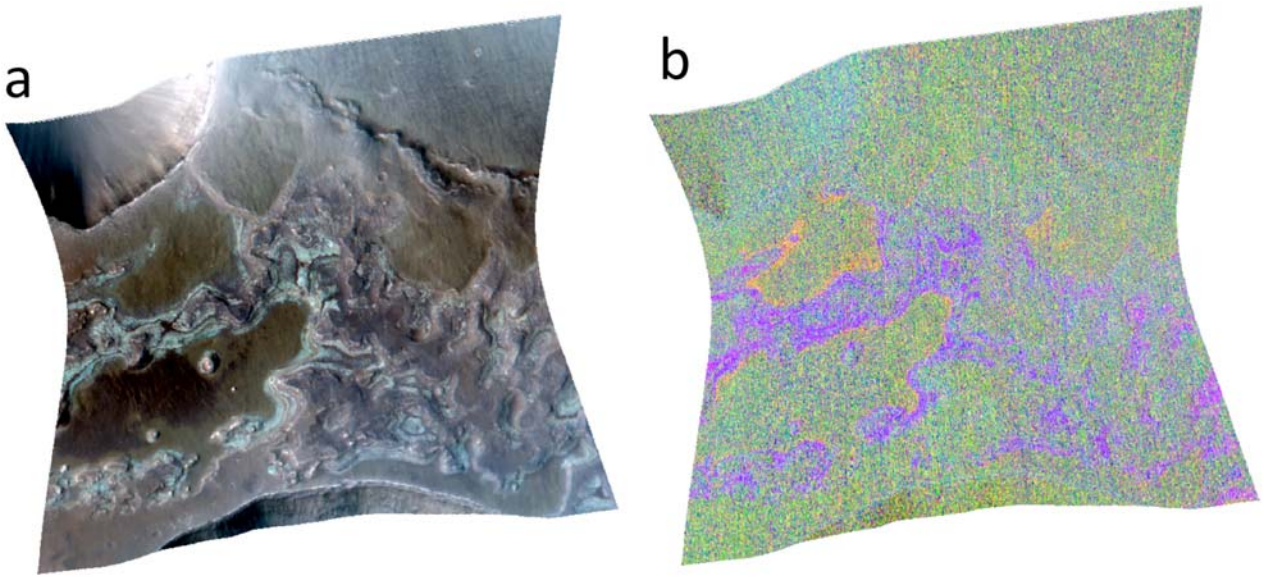

Figure 16. CRISM image FRT00005814 showing LLDs on the plateau northwest of Juventae: (a) false color IR image with R at 2.5 μm, G at 1.5 μm, and B at 1.1 μm, and (b) mineral indicator map showing two OH-bearing units in gold and magenta.

have also been observed in a pit on the plateau in a CRISM image [*Weitz et al.*, 2009] neighboring the region studied here.

5. Possible Formation Mechanisms for the Mounds Inside Juventae Chasma

[45] Three main models have been proposed for emplacement of the sulfate-bearing mounds in Juventae Chasma and are summarized here from previous studies [*Malin and Edgett*, 2000; *Chapman et al.*, 2003; *Catling et al.*, 2006]. One is that the chasma formed a large depression like a ''bathtub'' that was then infilled with sulfate-rich sediments. These sediments were then partially eroded over time, leaving as remnants four large separate bright mounds. This theory was discarded by *Catling et al.* [2006] as the height of mound C is above the height of the chasma walls and the volume of sulfate salt and water needed for this process is improbable. A second model is that four small depressions were formed and gradually infilled with sulfate-rich sediments over a long time period, followed by erosion of the substrate across the entire Juventae region, leaving these four ''buckets'' standing as raised mounds. A third model is that an extensive sulfate deposit predated the formation of Juventae Chasma. Portions of this sulfate deposit were exposed through the opening and erosion of the chasma, leaving three primary mounds. This sulfate deposit could have been a few hundred kilometers wide. Alternatively, there could be an enormous buried sulfate deposit thousands of kilometers wide that formed in a large lake or sea extending outward from Valles Marineris [*Malin and Edgett*, 2000] that just happens to be exposed where erosion at Juventae Chasma has punctured through overlying strata to reveal the sulfate layer below. For discussion in this paper we refer to these three theories as the ''bathtub'' hypothesis, the ''bucket'' hypothesis and the ''extensive unit'' hypothesis.

[46] Analysis of the sulfate stratigraphy in section 4.3 showed that kieserite and szomolnokite occur at roughly the same elevations in mounds A and B (Figure 8), but that the kieserite appeared to have been draped on top of the szomolnokite and eroded in places revealing the szomolnokite below at multiple elevations. Analysis of the CRISM spectra shows that the regions dominated by kieserite in mounds A and B are spectrally darker than the szomolnokite-bearing regions (Figures 9 and 11) and are layered with bright and dark material in HiRISE images. Similar textures, albedos, and elevations for the kieserite-bearing material at mounds A and B suggest a common formation process at these two mounds. This would be consistent with there having been a larger ''bucket'' in the western region of Juventae Chasma at one time that was then filled in with layers of szomolnokite, kieserite and polyhydrated sulfate. This is also completely consistent with deposition of regionally uniform sulfates in the ''bathtub'' hypothesis, where the ''bathtub'' covered the region consisting of mounds A and B. As mound B is currently much taller than mound A, and the PHS material is found at the top of mound B, it is reasonable that the PHS at the top of mound A has mostly eroded away. This PHS unit may have fragmented partially during the erosional process to leave regions where some PHS is mixed with the szomolnokite unit in mound A or parts of the monohydrated sulfates could have altered and hydrated over time.

[47] For mound C the absolute elevations of the strongest szomolnokite and kieserite spectral features are found lower in the mound, although mound C is taller than mounds A and B. The material at the top of mound C (Figures 4e, 4f, and 14) exhibits weaker sulfate signatures implying that other phases are intermixed with the sulfates in this mound. The szomolnokite and kieserite units are also more clearly separated by elevation (Figure 8) for mound C and the kieserite spectra are brighter than the szomolnokite

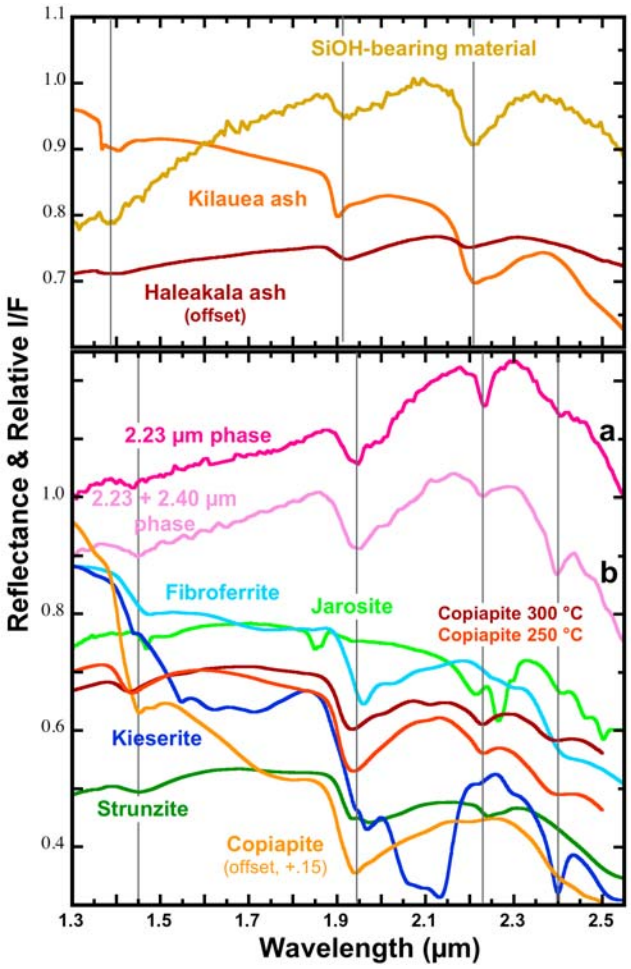

Figure 17. CRISM spectra from plateau region in image FRT00005814 compared with lab spectra of hydrated components (reflectance shown for lab samples, CRISM spectra are ratios and are offset for clarity). The gold spectrum was collected from the region shown in gold in Figure 16 and is compared to lab spectra of altered Kilauea ash containing opal-A [*Bishop et al.*, 2005] and altered Haleakala ash containing Al/Si-OH material [*Bishop et al.*, 2007b]. The magenta spectra are characterized by two dominant features. In some areas this unit contains a sharp and narrow band centered near 2.23 μm and a weak shoulder near 2.4 μm (spectrum a), while in other areas this unit contains a weaker band at 2.23 μm but a sharp band near 2.4 μm (spectrum b).

spectra for this mound (Figure 6) unlike mounds A and B. The spectral character and elevations of the sulfate minerals on mound C are sufficiently distinct from what is observed at mounds A and B that a separate formation event is likely.

[48] Mound D is again different in that the sulfate signatures are much weaker and imply mixing with other components or greater dust cover that obscures the sulfate spectral signatures. The kieserite units are again brighter than the szomolnokite units, similar to mound C, but different from mounds A and B. Although albedo differences could be attributed to a number of factors, the relative brightness of these units within the mounds may be related to their formation conditions. These data therefore support the bucket hypothesis, rather than the bathtub hypothesis. The extensive unit hypothesis would also be less likely here due to the differences in character of the sulfate deposits at mounds A–D; however, variations in brine concentration and grain morphology or depth could have existed and formed lateral transitions between facies of an extensive deposit. Mound D occurs at a much higher elevation than the other mounds and would be less likely to contain sulfates if the extensive unit hypothesis had taken place. Another problem with the extensive unit model is the presence of mafic outcrops in the chasma walls. If this process had occurred, a larger abundance of mound A–type material eroding out of the walls would be expected, although mass wasting along the wall rock could also be obscuring the ILD material within the walls, if present. Finally, downslope dipping of the strata at mound A suggest that this deposit was emplaced on top of the chasma wall and mound C occurs on top of chaotic terrain, both of which are consistent with sulfate deposition after the chasma formation (L. Wendt, personal communication, 2009). Thus, the extensive unit model is unlikely to have occurred.

[49] Evaporation of Fe/Mg-rich fluids formed through alteration of basalts has shown that Fe sulfates form when no olivine is present in the initial rock and that a combination of Fe and Mg sulfates form when olivine is present in the initial rock [*Tosca et al.*, 2005]. As olivine is present today in bedrock outcrops near the base of the mounds and in the wall rock, olivine can be presumed to have been present early in the region as well. Monohydrated sulfates could have precipitated out of the brine solution in the buckets and would have been fairly insoluble [*Kong et al.*, 1971]; however, formation of kieserite from amorphous Mg sulfate or dehydration of epsomite or hexahydrite requires elevated temperatures [*Freeman et al.*, 2007; *Wang et al.*, 2008]. Analyses of brine chemistry in Fe systems [*King and McSween*, 2005] indicates that if szomolnokite precipitated out of a brine system, then the minerals following this are expected to be more oxidized. A trend suggested by *King and McSween* [2005] is szomolnokite, copiapite, metahohmannite, jarosite, and schwertmannite. Thus, copiapite would be a likely PHS mineral formed after szomolnokite precipitation from the brine. However, this mineral scheme does not account for the kieserite. The presence of kieserite above the szomolnokite and below the PHS, might suggest that the PHS mineral is a Mg sulfate such as starkeyite.

[50] In summary, coordinated analyses of CRISM maps, MOLA elevations, and HiRISE images indicate that the kieserite-bearing unit tends to be located above the szomolnokite-bearing unit, especially for mound C. There is significant variance and overlap in the elevations of these two components for mounds A and B, suggesting a more complicated depositional process there. Possible origins for the mounds are considered: were these formed in multiple, small, and separate depositional events? Or was one large sulfate mound formed that was later eroded into separate mounds? Or is Juventae Chasma a window through the surface material into an expansive sulfate deposit emplaced by a large lake or ocean that was eroded into separate mounds? Although this cannot be conclusively answered, our data indicate that an expansive sulfate deposit is unlikely. The results of our mineralogy study are consistent with previous analyses of the geomorphology of the region that

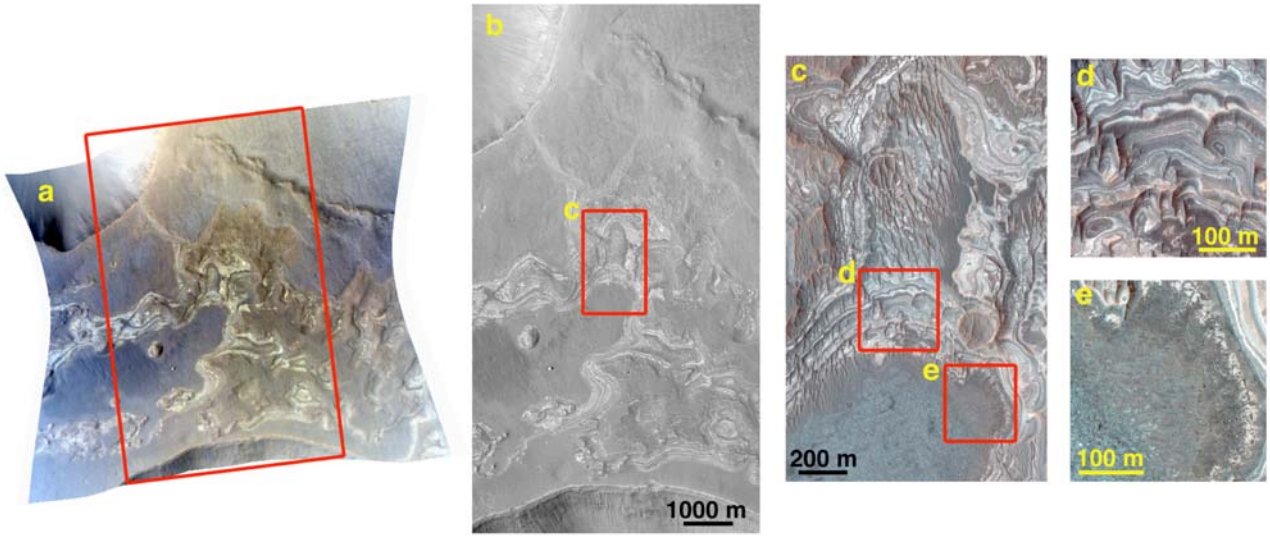

Figure 18. HiRISE image PSP_003434_1755 of the plateau region: (a) CRISM image FRT00005814 with a red box marking the region of (b) the full HiRISE image. (c) The locations of both of the textures illustrated in boxes Figures 18d and 18e. (d) The magenta colored material mapped in CRISM image FRT00005814 (Figure 16b and the spectra a and b in Figure 17 with a band at 2.23 μm due to hydroxylated ferric sulfate) exhibits the texture shown here. (e) The gold material in Figure 16b with spectral features resembling hydrated silica (Figure 17) has the broken and blocky texture of the material found below the hydroxylated ferric sulfate unit and above the bedrock.

contradict this theory [*Scott and Tanaka*, 1986; *Lucchitta et al.*, 1992; *Chapman and Tanaka*, 2001; *Chapman*, 2002]. The data are most consistent with mounds A and B having formed together and then eroded into separate mounds with mounds C and D having separate origins.

6. Possible Formation Processes for the Aqueous Units on the Plateau West of Juventae Chasma

[51] Silica has been predicted in sedimentary deposits on Mars by *McLennan* [2003] and a silica component has been suggested to be part of the surface material on Mars by TES [*Michalski et al.*, 2005]. It has been identified in the LLD material near several chasmata [*Milliken et al.*, 2008] and mixed with phyllosilicate outcrops at Mawrth Vallis [*Bishop et al.*, 2008; *McKeown et al.*, 2009]. Hydrated silica or opal has been found on Earth in a variety of altered ash and tephra deposits [*Christidis and Dunham*, 1993; *Morris et al.*, 2000; *Bishop et al.*, 2005; *Schiffman et al.*, 2006], in layered chalcedony deposits [e.g., *Wahlstrom*, 1941; *Heaney*, 1993] and has precipitated out of hydrothermal waters [*Renaut et al.*, 2002; *Bishop et al.*, 2004]. Hydrothermal precipitates of opal frequently form when thermal springs come in contact with cool water [*Renaut et al.*, 2002]. An opaline silica unit has been found in a relatively small region of the Juventae plateau shown in Figure 2b. CRISM images of other LLDs on the plateau have not shown this opaline silica phase; however, it is possible that the opal is more widespread on the Juventae plateau and simply covered by other materials. The opaline material described here could have formed via surface hydrothermal activity as in other places on Mars [*Squyres et al.*, 2008] and Earth [e.g., *Heaney*, 1994; *Morris et al.*, 2000; *Bishop et al.*, 2004; *Grenne and Slack*, 2005]. Subice volcanism is thought to have occurred in the region [*Chapman et al.*, 2003] and could have provided a heat source. The altered character of the opaline unit and its position underneath the hydroxylated ferric sulfate material (Figure 18) suggest separate aqueous events took place to form these mineralogies. Another possibility is that the opal and hydroxylated ferric sulfate layers were deposited sequentially during the same hydrothermal event as silica is less soluble and would have precipitated out first or the ferric sulfate deposit could have been leached to form the opaline layer beneath it [*Dove and Rimstidt*, 1994]. However, the texture of the two materials appears very different in the HiRISE images. This is consistent with a much older opal deposit or a much more friable opal deposit covered by a sulfate layer that is more resistant to erosion. Silica mobilization is also known to form horizontal opal deposits at anticlinal crests [e.g., *Medwedeff*, 1989] and thus the opal could have formed here via this mechanism, although there is no evidence for a hill here.

[52] The precise mineralogy of the partially hydrated sulfate material in the plateau west of Juventae Chasma is more of a mystery. This hydroxylated ferric sulfate found on the Juventae plateau occurs in beds that are each several meters thick and hundreds of meters long (Figure 16) [*Weitz et al.*, 2009]. As discussed in section 4.8, the composition of this phase is not yet well constrained, although the spectral features observed near 1.43–1.45, 1.94–1.95, 2.23, and 2.40 μm are characteristic of the dehydration products of copiapite (Figure 17b) [*Milliken et al.*, 2008], H_3O^+-jarosite [*Desborough et al.*, 2006], and szomolnokite [*Morris et al.*, 2009]. This material is not fully dehydrated because water bands are still present in the spectra. This absorption at 2.23 μm is attributed to the Fe^{3+}-OH site in close proximity

to sulfate. This mystery ferric sulfate hydroxide phase is not unique to the Juventae plateau region. *Lichtenberg et al.* [2009] have identified a similar spectral signature in CRISM spectra of Aram Chaos, a large crater east of Juventae Chasma.

[53] The PHS mineral copiapite is fairly soluble and frequently dissolves in the presence of water [*Hudson-Edwards et al.*, 1999]. If copiapite were present on the plateau, it could have been a precursor for the ferric sulfate phases currently present there, either by dehydrating to form a ferric sulfate hydroxide or by dissolving and providing a ferric sulfate brine for subsequent precipitation of a ferric sulfate hydroxide phase. The two aqueous phases described here on the Juventae plateau, together with other bedding forms in the region [*Mangold et al.*, 2008; *Weitz et al.*, 2009] are consistent with multiple aqueous events on the plateau.

7. Summary of Observations at Juventae Chasma

[54] Juventae Chasma contains four bright sulfate-bearing mounds inside the trough, mafic outcrops at the base of the mounds and in the wall rock, and finely bedded light-toned deposits on the plateau. Each of these materials was investigated using CRISM VNIR hyperspectral data, coordinated HiRISE and CTX images, and HRSC terrain models where available.

[55] In the sulfate mounds labeled A–D, the spectrally dominant sulfate phase is monohydrated. Most of the monohydrated sulfate signatures are consistent with szomolnokite ($FeSO_4 \cdot H_2O$) characterized by a water band near 2.08 μm, while some areas exhibit spectral features more similar to those of kieserite ($MgSO_4 \cdot H_2O$) with a band closer to 2.13 μm. The kieserite-bearing unit tends to be located above the szomolnokite-bearing unit, especially in mound C. There is significant variance in the elevations of these two compositions within mounds A and B, suggesting a more complicated history. The most extensive polyhydrated sulfate outcrops occur on the top of mound B, superposed on the monohydrated sulfate-bearing material. However, the polyhydrated sulfate outcrops cannot be uniquely assigned to a specific mineral.

[56] Three models for the origins of the mounds that were considered are that they are erosional remnants of a single deposit, that they formed in spatially disconnected basins, or that they are exposures of an extensive buried sulfate layer that predates Juventae chasma. Our results are inconsistent with a buried, extensive deposit and best explained by deposition of the mounds in spatially disconnected basins.

[57] Mafic minerals are observed in large outcrops in the wall rock that defines the chasma and smaller outcrops of wall rock spurs along the floor of the chasma. Distinct regions several kilometers across of material dominated by low-Ca pyroxene, high-Ca pyroxene, or olivine in the wall rock have been identified and comprise about 10% of the wall rock observed to date. The remaining 90% of the wall rock does not exhibit strong features characteristic of one of these minerals and is likely obscured by dust. Small outcrops ~50–500 m across of bedrock units dominated by low-Ca pyroxene or olivine were observed along the base of mound C.

[58] The plateau region northwest of Juventae Chasma is characterized by an abundance of finely bedded, light-toned layered deposits with associated inverted channels indicative of relict fluvial systems. Two different aqueous phases are identified in these layered materials on the surrounding plateau. An opaline silica phase, characterized by a broad Si-OH combination band centered near 2.21 μm, is found at the contact between the preexisting buried cratered surface and the bedded layered deposit. The overlying beds exposed in narrow ribbon-like outcrops exhibit a sharp Fe-OH combination band at 2.23 μm assigned to hydroxylated ferric sulfate. This unique feature has been observed in spectra of dehydrated copiapite, H_3O^+-jarosite, and szomolnokite sample, but is otherwise not commonly observed in mineral spectra. The surface of this component appears smooth in the HiRISE images compared to the cracked, fragmented and altered appearance of the opaline silica-bearing material just beneath it on the plateau. The bulk of the material comprising the surface of the Juventae plateau region appears to be dune sand and other aeolian material. The opaline silica and ferric sulfate hydroxide were likely formed in an acidic aqueous environment during the Hesperian period that was possibly associated with hydrothermal processes.

[59] **Acknowledgments.** The authors thank the MRO CRISM and HiRISE teams and the Mars Express HRSC Team for acquisition of the images used in this study, T. Hiroi for spectral measurements at RELAB at Brown University, L. Wendt for helpful discussions of the data, and M. Chapman and L. Le Deit for editorial suggestions that greatly improved the paper. Funding from MRO and MDAP (NNX06AD88) supported this work.

References

Anderson, J. H., Jr., and K. A. Wickersheim (1964), Near infrared characterization of water and hydroxyl groups on silica surfaces, *Surf. Sci.*, *2*, 252–260, doi:10.1016/0039-6028(64)90064-0.

Ansan, V., N. Mangold, P. Masson, E. Gailhardis, and G. Neukum (2008), Topography of valley networks on Mars from Mars Express High Resolution Stereo Camera digital elevation models, *J. Geophys. Res.*, *113*, E07006, doi:10.1029/2007JE002986.

Bishop, J. L., and E. Murad (2005), The visible and infrared spectral properties of jarosite and alunite, *Am. Mineral.*, *90*, 1100–1107, doi:10.2138/am.2005.1700.

Bishop, J. L., J. F. Mustard, C. M. Pieters, and T. Hiroi (1998), Recognition of minor constituents in reflectance spectra of ALH 84001 chips and the importance for remote sensing on Mars, *Meteorit. Planet. Sci.*, *33*, 693–698.

Bishop, J. L., E. Murad, M. D. Lane, and R. L. Mancinelli (2004), Multiple techniques for mineral identification on Mars: A study of hydrothermal rocks as potential analogues for astrobiology sites on Mars, *Icarus*, *169*, 311–323, doi:10.1016/j.icarus.2003.12.025.

Bishop, J. L., P. Schiffman, M. D. Lane, and M. D. Dyar (2005), Solfataric alteration in Hawaii as a mechanism for formation of the sulfates observed on Mars by OMEGA and the MER instruments, *Lunar Planet. Sci.*, *XXXVI*, Abstract 1456.

Bishop, J. L., et al. (2007a), Sulfates and mafic minerals in Juventae Chasma as seen by CRISM in coordination with OMEGA, HiRISE and Context images, in *Seventh International Conference on Mars, July 9–13, 2007, Pasadena CA* [CD-ROM], *LPI Contrib., 1353*, Abstract 3350.

Bishop, J. L., P. Schiffman, E. Murad, M. D. Dyar, A. Drief, and M. D. Lane (2007b), Characterization of alteration products in tephra from Haleakala, Maui: A visible-infrared spectroscopy, Mössbauer spectroscopy, XRD, EPMA and TEM Study, *Clays Clay Miner.*, *55*(1), 1–17, doi:10.1346/CCMN.2007.0550101.

Bishop, J. L., et al. (2008), Phyllosilicate diversity and past aqueous activity revealed at Mawrth Vallis, Mars, *Science*, *321*, 830–833, doi:10.1126/science.1159699.

Brown, A. J., and M. C. Storrie-Lombardi (2006), MR PRISM - A spectral analysis tool for the CRISM, *Proc. SPIE*, *6309*, Abstract 28, doi:10.1117/12.677107.

Catling, D. C., S. E. Wood, C. B. Leovy, D. R. Montgomery, H. M. Greenberg, C. R. Glein, and J. M. Moore (2006), Light-toned layered

deposits in Juventae Chasma, Mars, *Icarus*, *181*, 26–51, doi:10.1016/j.icarus.2005.10.020.

Chapman, M. G. (2002), Layered, massive, and thin sediments on Mars: Possible Late Noachian to Late Amazonian tephra?, in *Volcano–Ice Interactions on Earth and Mars*, edited by J. L. Smellie and M. G. Chapman, pp. 273–293, Geol. Soc., London.

Chapman, M. G., and J. L. Smellie (2007), Mars interior layered deposits and terrestrial sub-ice volcanoes compared: Observations and interpretations of similar geomorphic characteristics, in *The Geology of Mars: Evidence from Earth-Based Analogs*, edited by M. G. Chapman, pp. 178–210, Cambridge Univ. Press, U. K.

Chapman, M. G., and K. L. Tanaka (2001), Interior trough deposits on Mars: Subice volcanoes?, *J. Geophys. Res.*, *106*, 10,087–10,100.

Chapman, M. G., and K. L. Tanaka (2002), Related magma-ice interactions: Possible origin for chasmata, chaos, and surface materials in Xanthe, Margaritifer, and Meridiani Terrae, Mars, *Icarus*, *155*, 324–339, doi:10.1006/icar.2001.6735.

Chapman, M. G., M. T. Gudmundsson, A. J. Russell, and T. M. Hare (2003), Possible Juventae Chasma subice volcanic eruptions and Maja Valles ice outburst floods on Mars: Implications of Mars Global Surveyor crater densities, geomorpholoy, and topography, *J. Geophys. Res.*, *108*(E10), 5113, doi:10.1029/2002JE002009.

Christensen, P. R., et al. (2001), Mars Global Surveyor Thermal Emission Spectrometer experiment: Investigation description and surface science results, *J. Geophys. Res.*, *106*, 23,823–23,871.

Christidis, G., and A. C. Dunham (1993), Compositional variations in smectites: Part 1. Alteration of intermediate volcanic rocks. A case study from Milos Island, Greece, *Clay Miner.*, *28*, 255–273, doi:10.1180/claymin.1993.028.2.07.

Cloutis, E. A., et al. (2006), Detection and discrimination of sulfate minerals using reflectance spectroscopy, *Icarus*, *184*, 121–157.

Crowley, J. K., D. E. Williams, J. M. Hammarstrom, N. Piatak, I.-M. Chou, and J. C. Mars (2003), Spectral reflectance properties (0.4–2.5 μm) of secondary Fe-oxide, Fe-hydroxide, and Fe-sulphate-hydrate minerals associated with sulphide-bearing mine wastes, *Geochemistry: Explor. Environ. Anal.*, *3*, 219–228.

Desborough, G. A., K. S. Smith, H. A. Lowers, G. A. Swayze, J. M. Hammarstrom, S. F. Diehl, R. L. Driscoll, and R. W. Leinz (2006), The use of synthetic jarosite as an analog for natural jarosite, paper presented at Seventh International Conference on Acid Rock Drainage, Soc. for Min, Metall., and Explor., Saint Louis, Mo, 26–30 Mar.

Dove, P. M., and J. D. Rimstidt (1994), Silica-water interactions, in *Silica: Physical Behavior, Geochemistry and Materials Applications*, edited by P. J. Heaney et al., pp. 259–308, Mineral. Soc. of Am., Washington, D. C.

Freeman, J. J., A. Wang, and B. L. Joliff (2007), Pathways to form kieserite from epsomite at mid to low temperatures, with relevance to Mars, *Lunar and Planet. Sci.*, *XXXVIII*, Abstract 1298.

Gendrin, A., et al. (2005), Sulfates in Martian layered terrains: The OMEGA/Mars Express view, *Science*, *307*, 1587–1591, doi:10.1126/science.1109087.

Grenne, T., and J. F. Slack (2005), Geochemistry of jasper beds from the Ordovician Løkken Ophiolite, Norway: Origin of proximal and distal siliceous exhalites, *Econ. Geol.*, *100*(8), 1511–1527, doi:10.2113/1100.1518.1511.

Gwinner, K., F. Scholten, R. Jaumann, T. Roatsch, J. Oberst, and G. Neukum (2007), Global mapping of Mars by systematic derivation of Mars Express HRSC high-resolution digital elevation models and orthoimages, paper presented at ISPRS IV/7 Extraterrestrial Mapping Workshop, Lunar Planet. Inst., Houston, Tex.

Gwinner, K., T. Roatsch, K.-D. Matz, F. Scholten, S. Elgner, F. Preusker, J. Oberst, R. Jaumann, D. Heather, and G. Neukum (2008), Archival stereo data products of the HRSC experiment onboard Mars Express, *Lunar Planet. Sci.*, *XXXIX*, Abstract 2373.

Hauber, E., K. Gwinner, R. M. Stesky, F. Fueten, G. Michael, D. Reiss, H. Hoffmann, R. Jaumann, G. Neukum, and T. Zegers (2004), Interior layered deposits in Valles Marineris, Mars: Insights from 3D-data obtained by the High Resolution Stereo Camera (HRSC) on Mars Express, *Eos Trans. AGU*, *85*(47), Fall Meet. Suppl., Abstract V33C–1471.

Hawthorne, F. C., S. V. Krivovichev, and P. C. Burns (2000), The crystal chemistry of sulfate minerals, in *Sulfate Minerals: Crystallography, Geochemistry, and Environmental Significance*, edited by C. N. Alpers et al., *Rev. Mineral. Geochem.*, *40*, 1–112.

Heaney, P. J. (1993), A proposed mechanism for the growth of chalcedony, *Contrib. Mineral. Petrol.*, *115*, 66–74, doi:10.1007/BF00712979.

Heaney, P. J. (1994), Structure and chemistry of the low-pressure silica polymorphs, in *Silica: Physical Behavior, Geochemistry and Materials Applications*, edited by P. J. Heaney et al., pp. 1–40, Mineral. Soc. of Am., Washington, D. C.

Hudson-Edwards, K. A., C. Schell, and M. G. Macklin (1999), Mineralogy and geochemistry of alluvium contaminated by metal mining in the Rio Tinto area, southwest Spain, *Appl. Geochem.*, *14*(8), 1015–1030, doi:10.1016/S0883-2927(99)00008-6.

Jaumann, R., et al. (2007), The High Resolution Stereo Camera (HRSC) Experiment on Mars Express: Instrument aspects and experiment conduct from interplanetary cruise through nominal mission, *Planet. Space Sci.*, *55*, 928–952, doi:10.1016/j.pss.2006.12.003.

King, P. L., and H. Y. J. McSween (2005), Effects of H_2O, pH, and oxidation state on the stability of Fe minerals on Mars, *J. Geophys. Res.*, *110*, E12S10, 1–15, doi:10.1029/2005JE002482.

Komatsu, G., P. E. Geissler, R. G. Strom, and R. B. Singer (1993), Stratigraphy and erosional landforms of layered deposits in Valles Marineris, Mars, *J. Geophys. Res.*, *98*, 11,105–111,121, doi:10.1029/93JE00537.

Komatsu, G., G. G. Ori, P. Ciarcelluti, and Y. D. Yuri (2004), Interior layered deposits of Valles Marineris, Mars: Analogous sub-ice volcanism related to Baikal Rifting, southern Siberia, *Planet. Space Sci.*, *52*, 167–187, doi:10.1016/j.pss.2003.08.003.

Kong, P. C., T. W. Swaddle, and P. Bayliss (1971), The hydrothermal chemistry of some common transition metal compounds, *Can. J. Chem.*, *49*, 2442–2446, doi:10.1139/v71-398.

Kuzmin, R. O., M. V. Mironenko, and N. A. Evdokimova (2009), Spectral and thermodynamic constraints on the existence of gypsum at the Juventae Chasma on Mars, *Planet. Space Sci.*, *57*, 975–981, doi:10.1016/j.pss.2008.1012.1008.

Lane, M. D., J. L. Bishop, M. D. Dyar, P. L. King, M. Parente, and B. C. Hyde (2008), Mineralogy of the Paso Robles soils on Mars, *Am. Mineral.*, *93*, 728–739.

Le Deit, L., O. Bourgeois, S. Le Mouélic, D. Mège, J. P. Combe, C. Sotin, and M. Massé (2008), Light-toned layers on plateaus above Valles Marineris (Mars), *Lunar Planet. Sci.*, *XXXIX*, Abstract 1740.

Le Deit, L., O. Bourgeois, D. Mège, S. Le Mouélic, M. Massé, E. Hauber, R. Jaumann, and J.-P. Bibring (2009), Geological history of a light-toned formation draping the plateaus in the region of Valles Marineris, Mars, *Lunar Planet. Sci.*, *XL*, Abstract 1856.

Lichtenberg, K. A., R. E. Arvidson, R. V. Morris, S. L. Murchie, J. L. Bishop, T. D. Glotch, E. Noe Dobrea, J. F. Mustard, J. Andrews-Hanna, and L. H. Roach (2009), Stratigraphy and relationship of hydrated minerals in the layered deposits of Aram Chaos, Mars, *Lunar Planet. Sci.*, *XL*, Abstract 2326.

Lucchitta, B. K. (1982), Lakes or Playas in Valles Marineris, *NASA Tech. Memo., TM-85127*, 233–234 pp.

Lucchitta, B. K. (1990), Young volcanic deposits in the Valles, Marineris, Mars?, *Icarus*, *86*, 476–509, doi:10.1016/0019-1035(90)90230-7.

Lucchitta, B. K. (2005), Light layer and sinuous ridges on plateau near Juventae Chasma, Mars, *Lunar Planet. Sci.*, *XXXVI*, Abstract 1500.

Lucchitta, B. K., and M. G. Chapman (2002), Are the Valles Marineris giant volcano-tectonic depressions?, *Lunar Planet. Sci.*, *XXXIII*, Abstract 1689.

Lucchitta, B. K., A. S. McEwen, G. D. Clow, P. E. Geissler, R. B. Singer, R. A. Schultz, and S. W. Squyres (1992), The canyon system on Mars, in *Mars*, edited by H. H. Kieffer et al., pp. 453–492, Univ. of Ariz. Press, Tucson.

Lucchitta, B. K., N. K. Isbell, and A. Howington-Kraus (1994), Topography of Valles Marineris: Implications for erosional and structural history, *J. Geophys. Res.*, *99*, 3783–3798, doi:10.1029/93JE03095.

Malin, M. C., and K. S. Edgett (2000), Sedimentary rocks of early Mars, *Science*, *290*, 1927–1937, doi:10.1126/science.290.5498.1927.

Malin, M. C., and K. S. Edgett (2001), Mars Global Surveyor Mars Orbiter Camera: Interplanetary cruise through primary mission, *J. Geophys. Res.*, *106*, 23,429–23,570, doi:10.1029/2000JE001455.

Malin, M. C., et al. (2007), Context Camera Investigation on board the Mars Reconnaissance Orbiter, *J. Geophys. Res.*, *112*, E05S04, doi:10.1029/2006JE002808.

Mangold, N., V. Ansan, P. Masson, C. Quantin, and G. Neukum (2008), Geomorphic study of the fluvial landforms on the northern Valles Marineris plateau, Mars, *J. Geophys. Res.*, *113*, E08009, doi:10.1029/2007JE002985.

Mason, B., J. A. Nelen, P. Nuir, and S. R. Taylor (1975), The composition of the Chassigny meteorite, *Meteoritics*, *11*, 21–27.

McCauley, J. F. (1978), Geologic map of the Coprates Quadrangle of Mars, scale 1:5,000,000, *U.S. Geol. Surv. Misc. Invest. Map I-897*.

McEwen, A. S. (2009), The High Resolution Imaging Science Experiment (HiRISE) during MRO's primary science phase (PSP), *Icarus*, doi:10.1016/j.icarus.2009.04.023, in press.

McEwen, A. S., M. C. Malin, M. H. Carr, and W. K. Hartmann (1999), Voluminous volcanism on early Mars revealed in Valles Marineris, *Nature*, *397*, 584–586, doi:10.1038/17539.

McEwen, A. S., et al. (2007), Mars Reconnaissance Orbiter's High Resolution Imaging Science Experiment (HiRISE), *J. Geophys. Res.*, *112*, E05S02, doi:10.1029/2005JE002605.

McGuire, P. C., et al. (2008), CRISM retrieval of surface Lambert albedos for multispectral mapping of Mars with DISORT-based radiative transfer modeling, *IEEE Trans. Geosci. Remote Sens.*, *46*, 4020–4040, doi:10.1109/TGRS.2008.2000631.

McKeown, N. K., J. L. Bishop, E. Z. Noe Dobrea, M. Parente, B. L. Ehlmann, J. F. Mustard, S. L. Murchie, J.-P. Bibring, and E. Silver (2009), Characterization of phyllosilicates observed in the central Mawrth Vallis region, Mars, their potential formational processes, and implications for past climate, *J. Geophys. Res.*, doi:10.1029/2008JE003301, in press.

McLennan, S. M. (2003), Sedimentary silica on Mars, *Geology*, *31*(4), 315–318, doi:10.1130/0091-7613(2003)031<0315:SSOM>2.0.CO;2.

Medwedeff, D. A. (1989), Growth fault-bend folding at southeast Lost Hills, San Joaquin Valley, California, *AAPG Bull.*, *73*, doi:10.1306/1703C1309AE1306-1707-1311D1307-8645000102C8645001865D.

Michael, G., et al. (2005), Interior layered deposits in Coprates Chasma north wall and Juventae Chasma: Results from the Mars Express High Resolution Stereo Camera (HRSC) derived topography, *Geophys. Res. Abstr.*, *7*, 7439.

Michalski, J. R., M. D. Kraft, T. G. Sharp, L. B. Williams, and P. R. Christensen (2005), Mineralogical constraints on the high-silica Martian surface component observed by TES, *Icarus*, *174*, 161–177, doi:10.1016/j.icarus.2004.10.022.

Milliken, R. E., et al. (2008), Opaline silica in young deposits on Mars, *Geology*, *36*(11), 847–850, doi:10.1130/G24967A.24961.

Morris, R. V., H. V. Lauer Jr., C. A. Lawson, E. K. Gibson Jr., G. A. Nace, and C. Stewart (1985), Spectral and other physicochemical properties of submicron powders of hematite (α-Fe_2O_3), maghemite (γ-Fe_2O_3), magnetite (Fe_3O_4), goethite (α-FeOOH), and lepidocrocite (γ-FeOOH), *J. Geophys. Res.*, *90*, 3126–3144, doi:10.1029/JB090iB04p03126.

Morris, R. V., et al. (2000), Acid sulfate alteration products of a tholeiitic basalt: Implications for interpretation of Martian thermal emission spectra, *Lunar Planet. Sci.*, *XXXI*, Abstract 2014.

Morris, R. V., D. C. Golden, D. W. Ming, T. G. Graff, R. E. Arvidson, S. M. Wiseman, and K. A. Lichtenberg (2009), Visible and near-IR reflectance spectra for smectite, sulfate and perchlorate under dry conditions for interpretation of Martian surface mineralogy, *Lunar Planet. Sci.*, *XL*, Abstract 2317.

Murchie, S., et al. (2007), Compact Reconnaissance Imaging Spectrometer for Mars (CRISM) on Mars Reconnaissance Orbiter (MRO), *J. Geophys. Res.*, *112*, E05S03, doi:10.1029/2006JE002682.

Murchie, S. L., et al. (2009a), Evidence for the origin of layered deposits in Candor Chasma, Mars, from mineral composition and hydrologic modeling, *J. Geophys. Res.*, *114*, E00D05, doi:10.1029/2009JE003343.

Murchie, S. L., et al. (2009b), Compact Reconnaissance Imaging Spectrometer investigation and data set from the Mars Reconnaissance Orbiter's primary science phase, *J. Geophys. Res.*, *114*, E00D07, doi:10.1029/2009JE003344.

Nedell, S. S., S. W. Squyres, and D. W. Anderson (1987), Origin and evolution of the layered deposits in the Valles Marineris, *Icarus*, *70*, 409–441, doi:10.1016/0019-1035(87)90086-8.

Neukum, G., R. Jaumann, and HRSC Co-Investigator Team (2004), HRSC: The High Resolution Stereo Camera of Mars Express, in *Mars Express: The Scientific Payload*, edited by A. Wilson, pp. 17–35, Eur. Space Agency, Noordwijk, Netherlands.

Ori, G. G., G. Komatsu, A. Pacifici, E. Hauber, K. Gwinner, G. Neukum, and HRSC Co-Investigator Team (2006), Deltaic, sebkha and aeolian sedimentation in Juventae Chasma and their stratigraphic relationships (Mars), *Lunar Planet. Sci.*, *XXXVII*, Abstract 1247.

Parente, M. (2008), A new approach to denoising CRISM images, *Lunar Planet. Sci.*, *XXXIX*, Abstract 2528.

Parente, M., J. L. Bishop, and J. Cuadros (2008), Lab experiments to simulate coatings on phyllosilicate rocks and comparison with CRISM data of Mars, paper presented at First Workshop on Martian Phyllosilicates: Recorders of Aqueous Processes, Lunar and Planet. Inst., Paris.

Pelkey, S. M., et al. (2007), Parameterizing mineral diversity on mars from reflectance, *J. Geophys. Res.*, *112*, E08S14, doi:10.1029/2006JE002831.

Peterson, C. (1981), A secondary origin for the central plateau of Hebes Chasma, *Proc. Lunar Planet. Sci. Conf.*, *12th*, 1459–1471.

Renaut, R. W., B. F. Jones, J.-J. Tiercelin, and C. Tarits (2002), Sublacustrine precipitation of hydrothermal silica in rift lakes: Evidence from Lake Baringo, central Kenya Rift Valley, *Sediment. Geol.*, *148*, 235–257, doi:10.1016/S0037-0738(01)00220-2.

Roach, L. H., J. F. Mustard, S. L. Murchie, J.-P. Bibring, F. Forget, K. W. Lewis, O. Aharonson, M. Vincendon, and J. L. Bishop (2009a), Testing evidence of recent hydration state change in sulfates on Mars, *J. Geophys. Res.*, *114*, E00D02, doi:10.1029/2008JE003245.

Roach, L. H., J. F. Mustard, G. Swayze, R. E. Milliken, J. L. Bishop, S. L. Murchie, and K. Lichtenberg (2009b), Hydrated mineral stratigraphy of Ius Chasma, Valles Marineris, *Icarus*, doi:10.1016/j.icarus.2009.09.003, in press.

Rossi, A. P., G. Neukum, M. Pondrelli, S. van Gasselt, T. Zegers, E. Hauber, A. Chicarro, and B. Foing (2008), Large-scale spring deposits on Mars?, *J. Geophys. Res.*, *113*, E08016, doi:10.1029/2007JE003062.

Schiffman, P., R. A. Zierenberg, N. Marks, J. L. Bishop, and M. D. Dyar (2006), Acid fog deposition at Kilauea Volcano: A possible mechanism for the formation of siliceous-sulfate rock coatings on Mars, *Geology*, *34*(11), 921–924, doi:10.1130/G22620A.22621.

Scott, D. H., and K. L. Tanaka (1986), Geologic map of the western equatorial region of Mars, scale 1:15000000, *U.S. Geol. Surv. Misc. Invest. Map I-1802-A*.

Sharp, R. P. (1973), Mars: Fretted and chaotic terrain, *J. Geophys. Res.*, *78*, 4073–4083, doi:10.1029/JB078i020p04073.

Smith, D. E., et al. (2001), Mars Orbiter Laser Altimeter: Experiment summary after the first year of global mapping of Mars, *J. Geophys. Res.*, *106*, 23,689–623,722.

Squyres, S. W., et al. (2008), Detection of silica-rich deposits on Mars, *Science*, *320*, 1063–1067, doi:10.1126/science.1155429.

Sunshine, J. M., and C. M. Pieters (1993), Estimating modal abundances from the spectra of natural and laboratory pyroxene mixtures using the modified Gaussian model, *J. Geophys. Res.*, *98*, 9075–9087, doi:10.1029/93JE00677.

Sunshine, J. M., and C. M. Pieters (1998), Determining the composition of olivine from reflectance spectroscopy, *J. Geophys. Res.*, *103*, 13,675–613,688.

Tosca, N. J., S. M. McLennan, B. C. Clark, J. P. Grotzinger, J. A. Hurowitz, A. H. Knoll, C. Schröder, and S. W. Squyres (2005), Geochemical modeling of evaporation processes on Mars: Insight from the sedimentary record at Meridiani Planum, *Earth Planet. Sci. Lett.*, *240*, 122–148.

Treiman, A. H., K. H. Fuks, and S. Murchie (1995), Diagenetic layers in the upper walls of Valles Marineris, Mars: Evidence for drastic climate change since the mid-Hesperian, *J. Geophys. Res.*, *100*, 26,339–26,344, doi:10.1029/95JE03223.

Wahlstrom, E. E. (1941), Hydrothermal deposits in the Specimen Mountain volcanics, Rocky Mountain National Park, Colorado, *Am. Mineral.*, *26*, 551–561.

Wang, A., J. J. Freeman, and R. Arvidson (2008), Study of two structural polymorphs of MgSO4H2O by Raman, IR, XRD, and humidity buffer experiments: Implications for Martian kieserite, *Lunar Planet. Sci.*, *XXXIX*, Abstract 2172.

Weitz, C. M., T. J. Parker, F. S. Anderson, and J. A. Grant (2001), The interior layered deposits of Vallis Marineris: Layering, erosional processes, and age relationships, *Lunar Planet. Sci.*, *XXXII*, Abstract 1629.

Weitz, C. M., R. E. Milliken, J. A. Grant, A. S. McEwen, R. M. S. Williams, and J. L. Bishop (2008), Light-toned strata and inverted channels adjacent to Juventae and Ganges Chasmata, Mars, *Geophys. Res. Lett.*, *35*, L19202, doi:10.1029/2008GL035317.

Weitz, C. M., R. E. Milliken, J. A. Grant, A. S. McEwen, R. M. E. Williams, J. L. Bishop, and B. J. Thomson (2009), Mars Reconnaissance Orbiter observations of light-toned layered deposits and associated fluvial landforms on the plateaus adjacent to Valles Marineris, *Icarus*, doi:10.1016/j.icarus.2009.1004.1017, in press.

J. L. Bishop and A. J. Brown, Carl Sagan Center, SETI Institute, Mountain View, CA 94043, USA. (jbishop@seti.org)

W. M. Calvin, Department of Geological Sciences and Engineering, University of Nevada, Reno, NV 89557, USA.

P. C. McGuire, Department of Planetary Science and Remote Sensing, Freie Universitaet, D-12249 Berlin, Germany.

N. K. McKeown, Department of Earth and Planetary Sciences, University of California, Santa Cruz, CA 95064, USA.

R. Milliken and E. Z. Noe Dobrea, Jet Propulsion Laboratory, California Institute of Technology, Pasadena, CA 91109, USA.

S. L. Murchie, Johns Hopkins University Applied Physics Laboratory, Laurel, MD 20723, USA.

J. F. Mustard and L. H. Roach, Department of Geological Sciences, Brown University, Providence, RI 02912, USA.

M. Parente, Department of Electrical Engineering, Stanford University, Stanford, CA 94305, USA.

C. M. Rossi, Department of Aerospace Engineering, University of Michigan, Ann Arbor, MI 48109, USA.

C. M. Weitz, Planetary Science Institute, Tucson, AZ 85719, USA.